

# Insights from von Neumann analysis of high-order flux reconstruction schemes

P.E. Vincent\*, P. Castonguay, A. Jameson

Department of Aeronautics and Astronautics, Stanford University, Stanford, CA 94305, USA

## ARTICLE INFO

### Article history:

Received 29 January 2011

Received in revised form 21 June 2011

Accepted 8 July 2011

Available online 27 July 2011

### Keywords:

High-order methods

Flux reconstruction

Nodal discontinuous Galerkin method

Spectral difference method

Dispersion

Dissipation

## ABSTRACT

The flux reconstruction (FR) approach unifies various high-order schemes, including collocation based nodal discontinuous Galerkin methods, and all spectral difference methods (at least for a linear flux function), within a single framework. Recently, an infinite number of linearly stable FR schemes were identified, henceforth referred to as Vincent–Castonguay–Jameson–Huynh (VCJH) schemes. Identification of VCJH schemes offers significant insight into why certain FR schemes are stable (whereas others are not), and provides a simple prescription for implementing an infinite range of linearly stable high-order methods. However, various properties of VCJH schemes have yet to be analyzed in detail. In the present study one-dimensional (1D) von Neumann analysis is employed to elucidate how various important properties vary across the full range of VCJH schemes. In particular, dispersion and dissipation properties are studied, as are the magnitudes of explicit time-step limits (based on stability considerations). 1D linear numerical experiments are undertaken in order to verify results of the 1D von Neumann analysis. Additionally, two-dimensional non-linear numerical experiments are undertaken in order to assess whether results of the 1D von Neumann analysis (which is inherently linear) extend to real world problems of practical interest.

© 2011 Elsevier Inc. All rights reserved.

## 1. Introduction

Theoretical studies and numerical experiments suggest that unstructured high-order methods can provide solutions to otherwise intractable fluid flow problems within complex geometries. However, despite their potential benefits, the use of unstructured high-order methods remains limited in both academia and industry. There are various reasons for this situation. These include difficulties generating unstructured high-order meshes, problems resolving discontinuous solutions such as shock waves, and the relative complexity of unstructured high-order methods (compared with low-order schemes) [1].

In an effort to address the latter issue of complexity, Huynh proposed the flux reconstruction (FR) approach to high-order methods [2], which has been extended to triangular elements and used to solve the two-dimensional (2D) Euler equations by Wang and Gao [3]. The FR approach provides a simple and intuitive framework within which various well known high-order schemes can be cast. In particular, using the FR approach one can recover both collocation based nodal discontinuous Galerkin (DG) methods of the type described by Hesthaven and Warburton [4], and spectral difference (SD) methods (at least for a linear flux function), which were originally proposed by Kopriva and Koliás [5], and later generalized by Liu, Vinokur and Wang [6].

\* Corresponding author. Tel.: +1 650 724 5479; fax: +1 650 725 3377.

E-mail address: [pvincent@stanford.edu](mailto:pvincent@stanford.edu) (P.E. Vincent).

In addition to recovering known methods, the FR approach also facilitates the definition of new schemes. Huynh previously identified several new unstructured high-order methods using the FR approach [2,7]. Of particular note is the so called  $g_2$  method, which Huynh showed to be stable for various orders of accuracy (using von Neumann analysis), and which can be made more efficient than other FR methods via judicious placement of the solution points [2]. Additionally, Huynh proposed various guidelines for selecting the so called ‘flux correction function’, which determines numerous properties of the associated FR scheme. In particular, for one-dimensional (1D) FR schemes, Huynh suggested (based on von Neumann analysis) that if a flux correction function of degree  $k + 1$  is orthogonal to all polynomials of degree  $k - 2$  then the resulting scheme will be linearly stable. Recently, Vincent, Castonguay and Jameson proved this assertion to be true using an energy method [8], and consequently identified a range of FR schemes (parameterized by a single scalar), which are guaranteed to be linearly stable for all orders of accuracy. These linearly stable FR schemes will henceforth be referred to as Vincent–Castonguay–Jameson–Huynh (VCJH) schemes.

Identification of VCJH schemes represents a significant advance in terms of understanding why certain FR schemes are linearly stable, whereas others are not. However, the energy method employed by Vincent, Castonguay and Jameson (to prove linear stability) offers only limited insight into other properties of VCJH schemes. In the present study 1D von Neumann analysis is employed to elucidate how various important properties vary across the full range of VCJH schemes. The article begins with a brief review of the FR approach in 1D, followed by a summary of VCJH schemes in 1D. Two sections of analysis are then presented. The first investigates dispersion and dissipation properties of VCJH schemes, and the second investigates explicit time-step limits associated with VCJH schemes. Following this, two sets of numerical experiments are presented. The objective of the first set (which are 1D and linear) is to verify results of the 1D von Neumann analysis. The objective of the second set (which are 2D and non-linear) is to assess whether results of the 1D von Neumann analysis extend to real world problems of practical interest. Finally, conclusions are drawn.

## 2. The flux reconstruction approach

### 2.1. Overview

FR schemes are similar to nodal DG schemes, which are arguably the most popular type of unstructured high-order method (at least in the field of computational aerodynamics). Like nodal DG schemes, FR schemes utilize a high-order (nodal) polynomial basis to approximate the solution within each element of the computational domain, and like nodal DG schemes, FR schemes do not explicitly enforce inter-element solution continuity. However, unlike nodal DG schemes, FR methods are based solely on the governing system in a differential form. A description of the FR approach in 1D is presented below. For further information see the original paper of Huynh [2].

### 2.2. Preliminaries

Consider solving the following 1D scalar conservation law

$$\frac{\partial u}{\partial t} + \frac{\partial f}{\partial x} = 0 \tag{2.1}$$

within an arbitrary domain  $\Omega$ , where  $x$  is a spatial coordinate,  $t$  is time,  $u = u(x, t)$  is a conserved scalar quantity and  $f = f(u)$  is the flux of  $u$  in the  $x$  direction. Additionally, consider partitioning  $\Omega$  into  $N$  distinct elements, each denoted  $\Omega_n = \{x|x_n < x < x_{n+1}\}$ , such that

$$\Omega = \bigcup_{n=0}^{N-1} \Omega_n, \quad \bigcap_{n=0}^{N-1} \Omega_n = \emptyset. \tag{2.2}$$

The FR approach requires  $u$  is approximated in each  $\Omega_n$  by a function  $u_n^\delta = u_n^\delta(x, t)$ , which is a polynomial of degree  $k$  within  $\Omega_n$ , and identically zero elsewhere. Additionally, the FR approach requires  $f$  is approximated in each  $\Omega_n$  by a function  $f_n^\delta = f_n^\delta(x, t)$ , which is a polynomial of degree  $k + 1$  within  $\Omega_n$ , and identically zero elsewhere. Consequently, when employing the FR approach, a total approximate solution  $u^\delta = u^\delta(x, t)$  and a total approximate flux  $f^\delta = f^\delta(x, t)$  can be defined within  $\Omega$  as

$$u^\delta = \sum_{n=0}^{N-1} u_n^\delta \approx u, \quad f^\delta = \sum_{n=0}^{N-1} f_n^\delta \approx f, \tag{2.3}$$

where no level of inter-element continuity in  $u^\delta$  is explicitly enforced. However,  $f^\delta$  is required to be C0 continuous at element interfaces.

Note the requirement that each  $f_n^\delta$  is one degree higher than each  $u_n^\delta$ , which consequently ensures the divergence of  $f_n^\delta$  is of the same degree as  $u_n^\delta$  within  $\Omega_n$ .

### 2.3. Implementation

From an implementation perspective, it is advantageous to transform each  $\Omega_n$  to a standard element  $\Omega_S = \{\hat{x} | -1 \leq \hat{x} \leq 1\}$  via the mapping

$$\hat{x} = \Gamma_n(x) = 2 \left( \frac{x - x_n}{x_{n+1} - x_n} \right) - 1, \quad (2.4)$$

which has the inverse

$$x = \Gamma_n^{-1}(\hat{x}) = \left( \frac{1 - \hat{x}}{2} \right) x_n + \left( \frac{1 + \hat{x}}{2} \right) x_{n+1}. \quad (2.5)$$

Having performed such a transformation, the evolution of  $u_n^\delta$  within any individual  $\Omega_n$  (and thus the evolution of  $u^\delta$  within  $\Omega$ ) can be determined by solving the following transformed equation within the standard element  $\Omega_S$

$$\frac{\partial \hat{u}^\delta}{\partial t} + \frac{\partial \hat{f}^\delta}{\partial \hat{x}} = 0, \quad (2.6)$$

where

$$\hat{u}^\delta = \hat{u}^\delta(\hat{x}, t) = u_n^\delta \left( \Gamma_n^{-1}(\hat{x}), t \right) \quad (2.7)$$

is a polynomial of degree  $k$ ,

$$\hat{f}^\delta = \hat{f}^\delta(\hat{x}, t) = \frac{f_n^\delta \left( \Gamma_n^{-1}(\hat{x}), t \right)}{h_n}, \quad (2.8)$$

is a polynomial of degree  $k + 1$ , and  $h_n = (x_{n+1} - x_n)/2$ .

The FR approach to solving Eq. (2.6) within the standard element  $\Omega_S$  can be described in five stages. The first stage involves representing  $\hat{u}^\delta$  in terms of a nodal basis as follows

$$\hat{u}^\delta = \sum_{i=0}^k \hat{u}_i^\delta l_i, \quad (2.9)$$

where  $l_i$  are Lagrange polynomials defined as

$$l_i = \prod_{j=0, j \neq i}^k \left( \frac{\hat{x} - \hat{x}_j}{\hat{x}_i - \hat{x}_j} \right), \quad (2.10)$$

$\hat{x}_i$  ( $i = 0$  to  $k$ ) are  $k + 1$  distinct solution points within  $\Omega_S$ , and  $\hat{u}_i^\delta = \hat{u}_i^\delta(t)$  ( $i = 0$  to  $k$ ) are values of  $\hat{u}^\delta$  at the solution points  $\hat{x}_i$ . The second stage of the FR approach involves constructing a degree  $k$  polynomial  $\hat{f}^D = \hat{f}^D(\hat{x}, t)$ , defined as the approximate transformed discontinuous flux within  $\Omega_S$ . Specifically,  $\hat{f}^D$  is obtained via a collocation projection at the  $k + 1$  solution points, and can hence be expressed as

$$\hat{f}^D = \sum_{i=0}^k \hat{f}_i^D l_i \quad (2.11)$$

where the coefficients  $\hat{f}_i^D = \hat{f}_i^D(t)$  are simply values of the transformed flux at each solution point  $\hat{x}_i$  (evaluated directly from the approximate solution). The flux  $\hat{f}^D$  is termed discontinuous since it is calculated directly from the approximate solution, which is in general piecewise discontinuous between elements.

The third stage of the FR approach involves evaluating the approximate solution at either end of the standard element  $\Omega_S$  (i.e. at  $\hat{x} = \pm 1$ ). These values, in conjunction with analogous information from adjoining elements, are then used to calculate numerical interface fluxes. The exact methodology for calculating such numerical interface fluxes will depend on the nature of the equations being solved. For example, when solving the Euler equations one may use a Roe type approximate Riemann solver [9], or any other two-point flux formula that provides for an upwind bias. In what follows the numerical interface fluxes associated with the left and right hand ends of  $\Omega_S$  (and transformed appropriately for use in  $\Omega_S$ ) will be denoted  $\hat{f}_L^I$  and  $\hat{f}_R^I$  respectively.

The penultimate stage of the FR approach involves constructing the degree  $k + 1$  polynomial  $\hat{f}^C$ , by adding a correction flux  $\hat{f}^C = \hat{f}^C(\hat{x}, t)$  of degree  $k + 1$  to  $\hat{f}^D$ , such that their sum equals the transformed numerical interface flux at  $\hat{x} = \pm 1$ , yet in some sense follows  $\hat{f}^D$  within the interior of  $\Omega_S$ . In order to define  $\hat{f}^C$  such that it satisfies the above requirements, consider first defining degree  $k + 1$  correction functions  $g_L = g_L(\hat{x})$  and  $g_R = g_R(\hat{x})$  to approximate zero (in some sense) within  $\Omega_S$ , as well as satisfying

$$g_L(-1) = 1, \quad g_L(1) = 0, \quad (2.12)$$

$$g_R(-1) = 0, \quad g_R(1) = 1, \quad (2.13)$$

and

$$g_L(\hat{x}) = g_R(-\hat{x}). \tag{2.14}$$

A suitable expression for  $\hat{f}^C$  can now be written in terms of  $g_L$  and  $g_R$  as

$$\hat{f}^C = (\hat{f}_L^I - \hat{f}_L^D)g_L + (\hat{f}_R^I - \hat{f}_R^D)g_R, \tag{2.15}$$

where  $\hat{f}_L^D = \hat{f}^D(-1, t)$  and  $\hat{f}_R^D = \hat{f}^D(1, t)$ . Using this expression, the degree  $k + 1$  approximate transformed total flux  $\hat{f}^\delta$  within  $\Omega_S$  can be constructed from the discontinuous and correction fluxes as follows

$$\hat{f}^\delta = \hat{f}^D + \hat{f}^C = \hat{f}^D + (\hat{f}_L^I - \hat{f}_L^D)g_L + (\hat{f}_R^I - \hat{f}_R^D)g_R. \tag{2.16}$$

The final stage of the FR approach involves evaluating the divergence of  $\hat{f}^\delta$  at each solution point  $\hat{x}_i$  using the expression

$$\frac{\partial \hat{f}^\delta}{\partial \hat{x}}(\hat{x}_i) = \sum_{j=0}^k \hat{f}_j^D \frac{dI_j}{d\hat{x}}(\hat{x}_i) + (\hat{f}_L^I - \hat{f}_L^D) \frac{dg_L}{d\hat{x}}(\hat{x}_i) + (\hat{f}_R^I - \hat{f}_R^D) \frac{dg_R}{d\hat{x}}(\hat{x}_i). \tag{2.17}$$

These values can then be used to advance  $\hat{u}^\delta$  in time via a suitable temporal discretization of the following semi-discrete expression

$$\frac{d\hat{u}_i^\delta}{dt} = - \frac{\partial \hat{f}_i^\delta}{\partial \hat{x}}(\hat{x}_i). \tag{2.18}$$

### 2.4. Comments

The nature of a particular FR scheme depends solely on three factors, namely the location of the solution points  $\hat{x}_i$ , the methodology for calculating the interface fluxes  $\hat{f}_L^I$  and  $\hat{f}_R^I$ , and the form of the flux correction functions  $g_L$  (and thus  $g_R$ ). Huynh [2] showed previously that a collocation based nodal DG scheme is recovered in 1D if the corrections functions  $g_L$  and  $g_R$  are the right and left Radau polynomials respectively. Also, Huynh [2] showed that SD type methods can be recovered (at least for a linear flux function) if the correction functions  $g_L$  and  $g_R$  are set to zero at a set of  $k$  points within  $\Omega_S$  (located symmetrically about the origin). Several additional forms of  $g_L$  (and thus  $g_R$ ) have also suggested by Huynh [2,7], leading to the development of new schemes with various stability and accuracy properties.

## 3. Vincent–Castonguay–Jameson–Huynh schemes

### 3.1. Overview

VCJH schemes can be recovered if the corrections functions  $g_L$  and  $g_R$  are defined as

$$g_L = \frac{(-1)^k}{2} \left[ L_k - \left( \frac{\eta_k L_{k-1} + L_{k+1}}{1 + \eta_k} \right) \right], \tag{3.1}$$

and

$$g_R = \frac{1}{2} \left[ L_k + \left( \frac{\eta_k L_{k-1} + L_{k+1}}{1 + \eta_k} \right) \right], \tag{3.2}$$

where

$$\eta_k = \frac{c(2k + 1)(a_k k!)^2}{2}, \tag{3.3}$$

$$a_k = \frac{(2k)!}{2^k (k!)^2}, \tag{3.4}$$

$L_k$  is a Legendre polynomial of degree  $k$  (normalized to equal unity at  $\hat{x} = 1$ ), and  $c$  is a free scalar parameter that must lie within the range

$$c_- < c < c_\infty, \tag{3.5}$$

where

$$c_- = \frac{-2}{(2k + 1)(a_k k!)^2}, \tag{3.6}$$

and  $c_\infty = \infty$ .

Such correction functions ensure that if  $\Omega$  is periodic the resulting FR scheme will be linearly stable for any  $k$  in the broken Sobolev type norm  $\|u^\delta\|_{k,2}$ , defined as

$$\|u^\delta\|_{k,2} = \left[ \sum_{n=1}^N \int_{x_n}^{x_{n+1}} (u_n^\delta)^2 + \frac{c}{2} (h_n)^{2k} \left( \frac{\partial^k u_n^\delta}{\partial x^k} \right)^2 dx \right]^{1/2}. \quad (3.7)$$

For full details of how these schemes are derived see the original paper of Vincent, Castonguay and Jameson [8].

### 3.2. Recovery of known methods

Several known methods can be recovered from the range of VCJH schemes. In particular if  $c = c_{DG}$ , where

$$c_{DG} = 0, \quad (3.8)$$

then a collocation based nodal DG scheme is recovered [8]. Alternatively, if  $c = c_{SD}$  where

$$c_{SD} = \frac{2k}{(2k+1)(k+1)(a_k k!)^2}, \quad (3.9)$$

then an SD method is recovered (at least for a linear flux function) [8]. It is in fact the only SD method that can be recovered from the range of VCJH schemes. Further, it is identical to the SD scheme that Jameson [10] proved to be linearly stable, which is the same as the only SD scheme that Huynh found to be devoid of instabilities using von Neumann analysis [2]. Finally, if  $c = c_{HU}$  where

$$c_{HU} = \frac{2(k+1)}{(2k+1)k(a_k k!)^2}, \quad (3.10)$$

then a so called  $g_2$  FR method is recovered [8]. Such a scheme was originally identified by Huynh [2] to be particularly stable, and can be made more efficient than other FR methods via judicious placement of the solution points. For further details see the original paper of Huynh [2].

## 4. Dispersion and dissipation properties of Vincent–Castonguay–Jameson–Huynh schemes

### 4.1. Overview

A successful unstructured high-order method must accurately capture the propagation of waves and other transient features within complex geometries. Consequently, the dispersion and dissipation properties of VCJH schemes deserve particular attention. The objective of the following section is to determine how dispersion and dissipation properties vary over the full range of VCJH schemes. In line with previous studies [2,11–16], this is achieved using 1D von Neumann analysis. Specifically, traveling wave solutions with a prescribed spatial periodicity at the inter-element level are identified and analyzed. In the physics community, such solutions are commonly referred to as Bloch waves, an expose of which can be found in the solid-state physics textbook of Ibach and Lüth [17], for example. Dispersion and dissipation relations for these Bloch wave solutions are obtained and analyzed. In particular, via comparison with the dispersion and dissipation relations for exact plane wave solutions (of a linear conservation law), a theoretical (global) order of accuracy associated with dispersion and dissipation errors is obtained for VCJH schemes.

### 4.2. Theory

#### 4.2.1. Preliminaries

Consider that  $f = au$  where  $a$  is a constant scalar. Further, for notational convenience (but without significant loss of generality) consider that  $a = 1$ . Under such assumptions, Eq. (2.1) can be written as

$$\frac{\partial u}{\partial t} + \frac{\partial u}{\partial x} = 0, \quad (4.1)$$

which admits plane wave solutions of the form

$$u = e^{i(\theta x - \omega t)}, \quad (4.2)$$

provided the temporal frequency  $\omega = \omega(\theta)$  satisfies

$$Re(\omega) = \theta, \quad (4.3)$$

and

$$Im(\omega) = 0, \quad (4.4)$$

where  $\theta$  is a real prescribed wave number, and  $I = \sqrt{-1}$ . Eqs. (4.3) and (4.4) are known as dispersion and dissipation relations respectively for the exact plane wave solutions described by Eq. (4.2).

Consider now that all elements  $\Omega_n$  of the domain  $\Omega$  have a fixed width  $h_n = h$ . Further, for notational convenience (but without significant loss of generality) consider that  $h = 1$ . Under such assumptions a FR semi-discretization of Eq. (4.1) within the standard element  $\Omega_s$  can be written as

$$\frac{d\hat{\mathbf{u}}^\delta}{dt} = -2 \sum_{j=0}^k \hat{u}_j^\delta \frac{dl_j}{d\hat{x}}(\hat{x}_i) - (\hat{f}_L^l - 2\hat{u}_L^\delta) \frac{dg_L}{d\hat{x}}(\hat{x}_i) - (\hat{f}_R^l - 2\hat{u}_R^\delta) \frac{dg_R}{d\hat{x}}(\hat{x}_i), \tag{4.5}$$

where  $\hat{u}_L^\delta = \hat{u}^\delta(-1, t)$ , and  $\hat{u}_R^\delta = \hat{u}^\delta(1, t)$ . Further, if the interface fluxes are all considered to be fully upwind, then Eq. (4.5) can be written as

$$\frac{d\hat{\mathbf{u}}^\delta}{dt} = -2 \sum_{j=0}^k \hat{u}_j^\delta \frac{dl_j}{d\hat{x}}(\hat{x}_i) - (\hat{f}_L^l - 2\hat{u}_L^\delta) \frac{dg_L}{d\hat{x}}(\hat{x}_i), \tag{4.6}$$

where  $\hat{f}_L^l$  now depends solely on data upwind of the element currently represented within  $\Omega_s$ . On rewriting Eq. (4.6) in matrix-vector form one obtains

$$\frac{d\hat{\mathbf{u}}^\delta}{dt} = -2\mathbf{D}\hat{\mathbf{u}}^\delta - (\hat{f}_L^l - 2\hat{u}_L^\delta) \mathbf{g}_{\hat{x}L}, \tag{4.7}$$

where

$$\hat{\mathbf{u}}^\delta[i] = \hat{u}_i^\delta, \quad \mathbf{D}[i, j] = \frac{dl_j}{d\hat{x}}(\hat{x}_i), \quad \mathbf{g}_{\hat{x}L}[i] = \frac{dg_L}{d\hat{x}}(\hat{x}_i), \tag{4.8}$$

which can be written as

$$\frac{d\hat{\mathbf{u}}^\delta}{dt} = -2\mathbf{D}\hat{\mathbf{u}}^\delta - (\hat{f}_L^l - 2\mathbf{1}^T \hat{\mathbf{u}}^\delta) \mathbf{g}_{\hat{x}L}, \tag{4.9}$$

where

$$\mathbf{1}[i] = I_i(-1). \tag{4.10}$$

#### 4.2.2. Identifying Bloch wave solutions

Consider identifying Bloch wave solutions of Eq. (4.9). Specifically, consider identifying solutions within  $\Omega$  that when mapped from each  $\Omega_n$  are represented as follows within the standard element  $\Omega_s$

$$\hat{\mathbf{u}}^\delta = e^{I(n\bar{\theta}^\delta - \omega^\delta t)} \hat{\mathbf{v}}^\delta, \tag{4.11}$$

where  $\bar{\theta}^\delta$  is a prescribed baseline wavenumber within the range  $-\pi \leq \bar{\theta}^\delta \leq \pi$ ,  $\omega^\delta$  is a temporal frequency (to be determined), and  $\hat{\mathbf{v}}^\delta$  is a vector (to be determined) that is independent of the element  $\Omega_n$  under consideration. The modifier ‘baseline’ proceeds the word ‘wavenumber’ in the previous sentence because although  $-\pi \leq \bar{\theta}^\delta \leq \pi$ , the true wavenumber of solutions described by Eq. (4.11) may in fact be higher, due to the extra (intra-element) degrees of freedom within  $\hat{\mathbf{v}}^\delta$ , which defines a polynomial of degree  $k$  within the standard element. This fact is particularly important when forming dispersion and dissipation relations for the Bloch wave solutions, and will be discussed again shortly.

For solutions of the type described by Eq. (4.11), the fully upwind interface flux  $\hat{f}_L^l$  in Eq. (4.9) can be written as

$$\hat{f}_L^l = 2\mathbf{r}^T e^{I(n\bar{\theta}^\delta - \bar{\theta}^\delta - \omega^\delta t)} \hat{\mathbf{v}}^\delta, \tag{4.12}$$

where

$$\mathbf{r}[i] = I_i(1). \tag{4.13}$$

On substituting Eqs. (4.11) and (4.12) into Eq. (4.9) one obtains

$$\mathbf{Q}\hat{\mathbf{v}}^\delta = \omega^\delta \hat{\mathbf{v}}^\delta, \tag{4.14}$$

where

$$\mathbf{Q} = -2I \left[ \mathbf{D} + \mathbf{g}_{\hat{x}L} (\mathbf{r}^T e^{-I\bar{\theta}^\delta} - \mathbf{1}^T) \right]. \tag{4.15}$$

For a given FR scheme  $\mathbf{Q}$  depends solely on the baseline wave number  $\bar{\theta}^\delta$ . It is clear from Eq. (4.14) that in order for Eq. (4.11) to represent an admissible solution of Eq. (4.9),  $\omega^\delta$  must be an eigenvalue of  $\mathbf{Q}$ , and  $\hat{\mathbf{v}}^\delta$  must be an associated eigenvector. Therefore,  $\mathbf{Q}$  and hence (for a given FR scheme) a baseline wavenumber  $\bar{\theta}^\delta$ , is associated with  $k + 1$  admissible solutions (since  $\mathbf{Q}$  is of dimension  $k + 1$ , and hence has  $k + 1$  associated eigenvalue/eigenvector pairs). The association of multiple admissible solutions, and hence multiple admissible values of  $\omega^\delta$ , with a single baseline wavenumber  $\bar{\theta}^\delta$  appears to be interpreted in various ways by different authors. It is often stated that  $k$  of the  $k + 1$  admissible solutions are ‘spurious’ modes, which should

be dismissed. However, each of the  $k + 1$  admissible solutions must be considered if one is to construct full dispersion and dissipation relations, as will be discussed next.

#### 4.2.3. Identifying dispersion and dissipation relations

The association of a single baseline wavenumber  $\bar{\theta}^\delta$  with multiple admissible solutions, and hence multiple admissible values of  $\omega^\delta$  is clearly interpreted by Van den Abeele [12], who points out that each admissible Bloch wave solution associated with a given  $\bar{\theta}^\delta$  actually has a (unique) true wavenumber  $\theta^\delta$  in the range  $-(k + 1)\pi \leq \theta^\delta \leq (k + 1)\pi$ , which depends on both the baseline wavenumber  $\bar{\theta}^\delta$ , and the form of  $\hat{\mathbf{v}}^\delta$  associated with the admissible solution. Specifically, as explained by Van den Abeele [12], the true wavenumber  $\theta^\delta$  of a particular admissible solution is given by  $\theta^\delta = \bar{\theta}^\delta + l2\pi$  for some integer  $l$  such that  $-(k + 1)\pi \leq \theta^\delta \leq (k + 1)\pi$ , where the specific value of  $l$  depends on the vector  $\hat{\mathbf{v}}^\delta$  associated with the admissible solution in question. In the work of Van den Abeele [12] the true wavenumber  $\theta^\delta$  of an admissible solution was identified visually (by plotting the form of  $\hat{\mathbf{v}}^\delta$ , which defines a polynomial of degree  $k$  within the standard element). In the present study an automated procedure was employed based on a modal analysis of the polynomial defined by  $\hat{\mathbf{v}}^\delta$ . For a given FR scheme the main stages of the procedure can be outlined as follows:

1. For a given  $\bar{\theta}^\delta$  form the matrix  $\mathbf{Q}$ , and identify the  $k + 1$  admissible solutions associated with  $\bar{\theta}^\delta$ .
2. For each of the  $k + 1$  admissible solutions, represent the polynomial defined by  $\hat{\mathbf{v}}^\delta$  in terms of a modal Legendre basis.
3. Start a counter at  $n = 0$ .
4. Discount  $n$  of the  $k + 1$  admissible solutions for which true wavenumbers have already been identified. Of the remaining admissible solutions, identify the one with  $\hat{\mathbf{v}}^\delta$  that defines a polynomial with the most energized  $n^{\text{th}}$  order Legendre basis function.
5. Associate this admissible solution with a true wavenumber  $\theta^\delta = \bar{\theta}^\delta + l2\pi$ , where  $l$  is chosen such that  $|\bar{\theta}^\delta + l2\pi|$  is minimized, with the restriction that  $\theta^\delta$  cannot be equal a true wavenumber that has been previously assigned.
6.  $n = n + 1$ .
7. If  $n = k$  stop the process, since a true wavenumber  $\theta^\delta$  will have been identified for each of the  $k + 1$  admissible solutions associated with  $\bar{\theta}^\delta$ . If  $n \neq k$  go back to step four and continue the process.

Application of the above procedure to a sampling of  $\bar{\theta}^\delta$  in the range  $-\pi \leq \bar{\theta}^\delta \leq \pi$  will result in associating a sampling of  $\theta^\delta$  in the range  $-(k + 1)\pi \leq \theta^\delta \leq (k + 1)\pi$  with unique values of  $\omega^\delta$ . Hence, the procedure can be used to (indirectly) obtain a function  $\omega^\delta(\theta^\delta)$  for Bloch wave solutions, from which associations between  $Re(\omega^\delta)$  and  $\theta^\delta$  (dispersion relations) and  $Im(\omega^\delta)$  and  $\theta^\delta$  (dissipation relations) can be easily obtained.

#### 4.2.4. Quantifying orders of accuracy

For Bloch wave solutions of Eq. (4.9), consider defining a combined dispersion and dissipation error  $E_T = E_T(\theta^\delta)$  as

$$E_T = |\omega^\delta(\theta^\delta) - \omega(\theta^\delta)|. \quad (4.16)$$

Following the approach of Huynh [2] a theoretical (global) order of accuracy  $A_T$  associated with dispersion and dissipation errors can be defined for a given FR scheme in terms of  $E_T$  as follows

$$A_T = \left( \frac{\ln[E_T(\theta_R^\delta)] - \ln[E_T(\theta_R^\delta/2)]}{\ln(2)} \right) - 1, \quad (4.17)$$

where  $\theta_R^\delta$  is a true wavenumber chosen such that  $E_T$  remains small (*i.e.* it is a wavenumber that is well resolved by the FR scheme). The results of Atkins and Helenbrook [18] suggest  $A_T$  will determine how well the FR scheme can model various processes, including wave propagation, long-time instability dynamics, and the evolution of natural phenomena that depend weakly on initial conditions. In particular, Atkins and Helenbrook [18] show (for DG schemes) that the order of accuracy associated with dispersion and dissipation errors corresponds directly to the order of accuracy with which the schemes can resolve vortex shedding from a cylinder (when solving the Navier-Stokes equations).

### 4.3. Results and discussion

#### 4.3.1. Dispersion and dissipation relations

Figs. 1 and 2 plot dispersion and dissipation relations for Bloch wave solutions of Eq. (4.9) for various VCJH schemes. All VCJH schemes considered had solution points at the Gauss points and  $k = 3$ . Plots for other values of  $k$  are qualitatively similar, and are hence omitted for brevity. Also, since dispersion relations are anti-symmetric, and dissipation relations are symmetric, only results for  $\theta^\delta > 0$  are presented. For reference, dispersion relations for the exact plane wave solutions described by Eq. (4.2) are marked with dashed gray lines in Fig. 1, and the related dissipation relations for exact plane wave solutions are marked with dashed gray lines in Fig. 2.

The plots in Figs. 1 and 2 encode a significant amount of information. An extensive analysis is beyond the scope of this particular study. However, several important observations can be made. Firstly, it can be noted that for all VCJH schemes,  $Im(\omega^\delta) \leq 0$  for all  $\theta^\delta$ . Therefore all VCJH schemes are dissipative, at least for a linear flux function. Such a result is expected

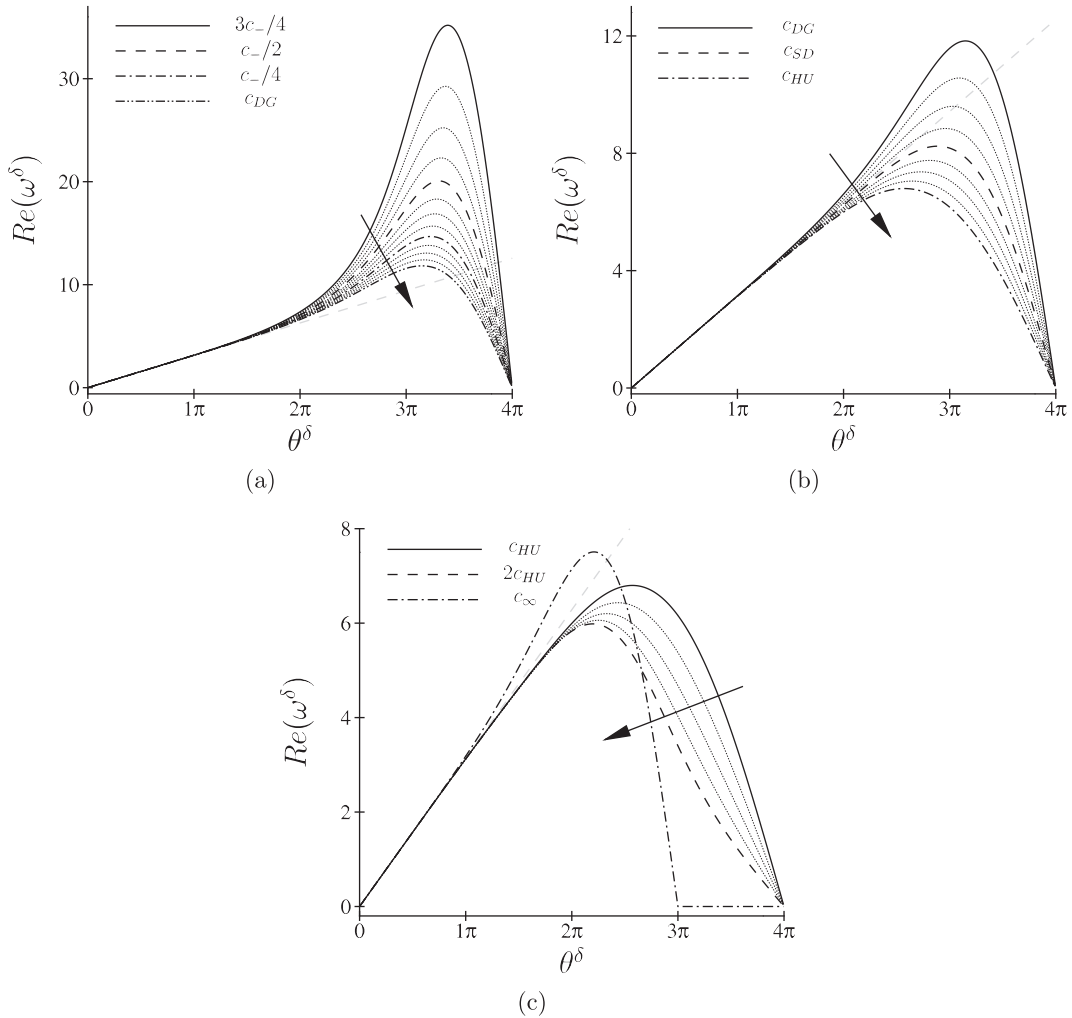


**Fig. 1.** Plots of dispersion relations for Bloch wave solutions of the form described by Eq. (4.11) (for various VCJH schemes when  $k = 3$ ). Dispersion relations for  $3c_-/4 \leq c \leq c_{DG}$  are shown in (a), dispersion relations for  $c_{DG} \leq c \leq c_{HU}$  are shown in (b), and dispersion relations for  $c_{HU} \leq c \leq c_\infty$  are shown in (c). In all plots, thin dotted black lines correspond to (linearly spaced) intermediate values of  $c$ , and the arrows indicate (qualitatively) a direction of increasing  $c$ . The dashed gray lines mark the dispersion relation for the exact plane wave solutions described by Eq. (4.2).

due to the inherent linear stability of VCJH schemes. Secondly, it can be noted that in the limit  $c \rightarrow c_-$  the range of  $\theta^\delta$  over which the Bloch wave dispersion relation reasonably approximates the exact dispersion relation decreases. However, the range of  $\theta^\delta$  over which the Bloch wave dissipation relation reasonably approximates the exact dissipation relation increases. Consequently, in the limit  $c \rightarrow c_-$ , undamped high wavenumber solutions with erroneous dispersion relations are admitted. Such behavior is clearly unfavorable, and use of such schemes should be avoided. Thirdly, it can be noted that for values of  $c$  in the range  $c_{DG} \leq c \leq c_{HU}$  (i.e. values of  $c$  encompassing those associated with known schemes) the range of  $\theta^\delta$  over which the Bloch wave dispersion relation reasonably approximates the exact dispersion relation changes in a non-monotonic fashion. In particular, it appears that the Bloch wave dispersion relation reasonably approximates the exact dispersion relation over an approximately maximal range of  $\theta^\delta$  when  $c = c_{SD}$ . Additionally, for values of  $c$  in the range  $c_{DG} \leq c \leq c_{HU}$ , it can be noted that high wavenumber Bloch wave solutions with erroneous dispersion relations are damped. Such behavior is favorable. Finally, it can be noted that in the limit  $c \rightarrow c_\infty$  both the Bloch wave dispersion and Bloch wave dissipation relations tend to zero for high wavenumbers. Consequently, in the limit  $c \rightarrow c_\infty$  high wavenumber solutions will neither move, nor decay in time. Such behavior (which is in line with previous observations made by Vincent, Castonguay and Jameson [8]) is clearly unfavorable, and use of such schemes should be avoided.

#### 4.3.2. Order of accuracy

Fig. 3 illustrates how  $A_T$  varies across a range of VCJH schemes various values of  $k$ . All VCJH schemes considered had solution points at the Gauss points. The  $c$  axis is on a linear scale so that behavior for negative values of  $c$  can be plotted. Fig. 4

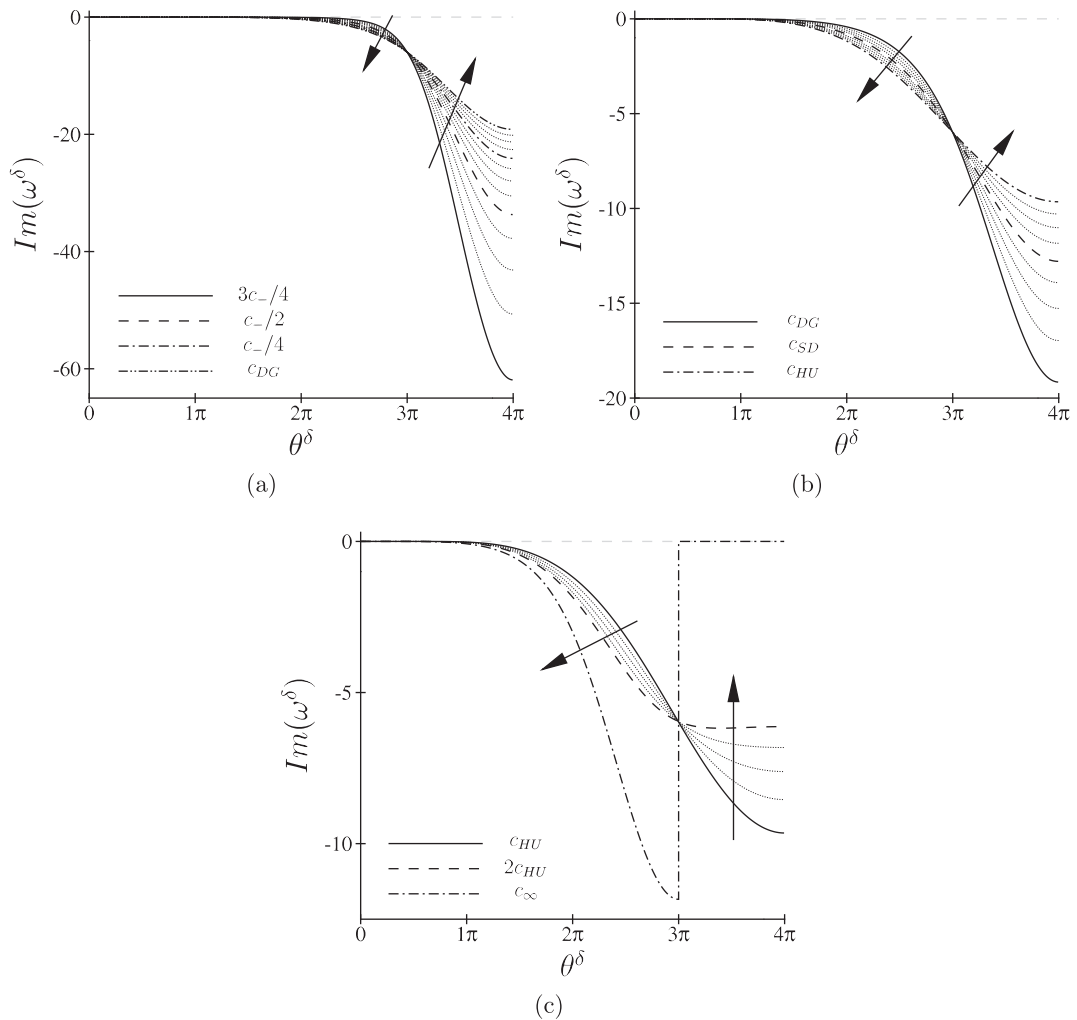


**Fig. 2.** Plots of dissipation relations for Bloch wave solutions of the form described by Eq. (4.11) (for various VCJH schemes when  $k = 3$ ). Dissipation relations for  $3c_-/4 \leq c \leq c_{DC}$  are shown in (a), dissipation relations for  $c_{DC} \leq c \leq c_{HU}$  are shown in (b), and dissipation relations for  $c_{HU} \leq c \leq c_\infty$  are shown in (c). In all plots, thin dotted black lines correspond to (linearly spaced) intermediate values of  $c$ , and the arrows indicate (qualitatively) a direction of increasing  $c$ . The dashed gray lines mark the dissipation relation for the exact plane wave solutions described by Eq. (4.2).

also plots  $A_T$  against  $c$  for various values of  $k$ . However, the  $c$  axis is on a log scale, so that behavior over a larger range of  $c$  can be plotted. In both Figs. 3 and 4,  $A_T$  was obtained using a value of  $\theta_R^\delta = \pi/8$  when  $k = 2$ , a value of  $\theta_R^\delta = \pi/4$  when  $k = 3$ , a value of  $\theta_R^\delta = \pi/3$  when  $k = 4$ , and a value of  $\theta_R^\delta = 2\pi/3$  when  $k = 5$ .

It is clear from Figs. 3 and 4 that for all values of  $k$ , and for all VCJH schemes,  $A_T$  exhibits a level of super accuracy (*i.e.* for all values of  $k$ , and for all VCJH schemes,  $A_T > k + 1$ ). Moreover, it is clear that  $A_T$  varies non-monotonically with  $c$ . Specifically, for all values of  $k$ , a maximal value of  $A_T \approx 2k + 1$  is attained when  $c = c_{DC}$ . Such a result is in line with the findings of Huynh [2]. Also, there exists a plateau of  $A_T \approx 2k$  on which VCJH schemes with  $c = c_{SD}$  and  $c = c_{HU}$  both reside. Such a result is also in line with the findings of Huynh [2]. Finally, it can be noted that  $A_T \approx 2k$  as  $c$  approaches  $c_-$ , and  $A_T \approx 2k - 1$  as  $c$  approaches  $c_\infty$ .

## 5. Explicit time-step limits associated with Vincent–Castonguay–Jameson–Huynh schemes

### 5.1. Overview

When using an explicit temporal discretization, the time-step size is limited by a stability constraint, known as a Courant–Friedrichs–Lewy (CFL) limit. Such a limit is often more restrictive than any imposed by accuracy requirements, and unfortunately may become prohibitively severe if a high-order spatial discretization is employed (since the CFL limit typically scales as the inverse of the spatial order squared [19]). Such issues have often lead researchers to combine implicit

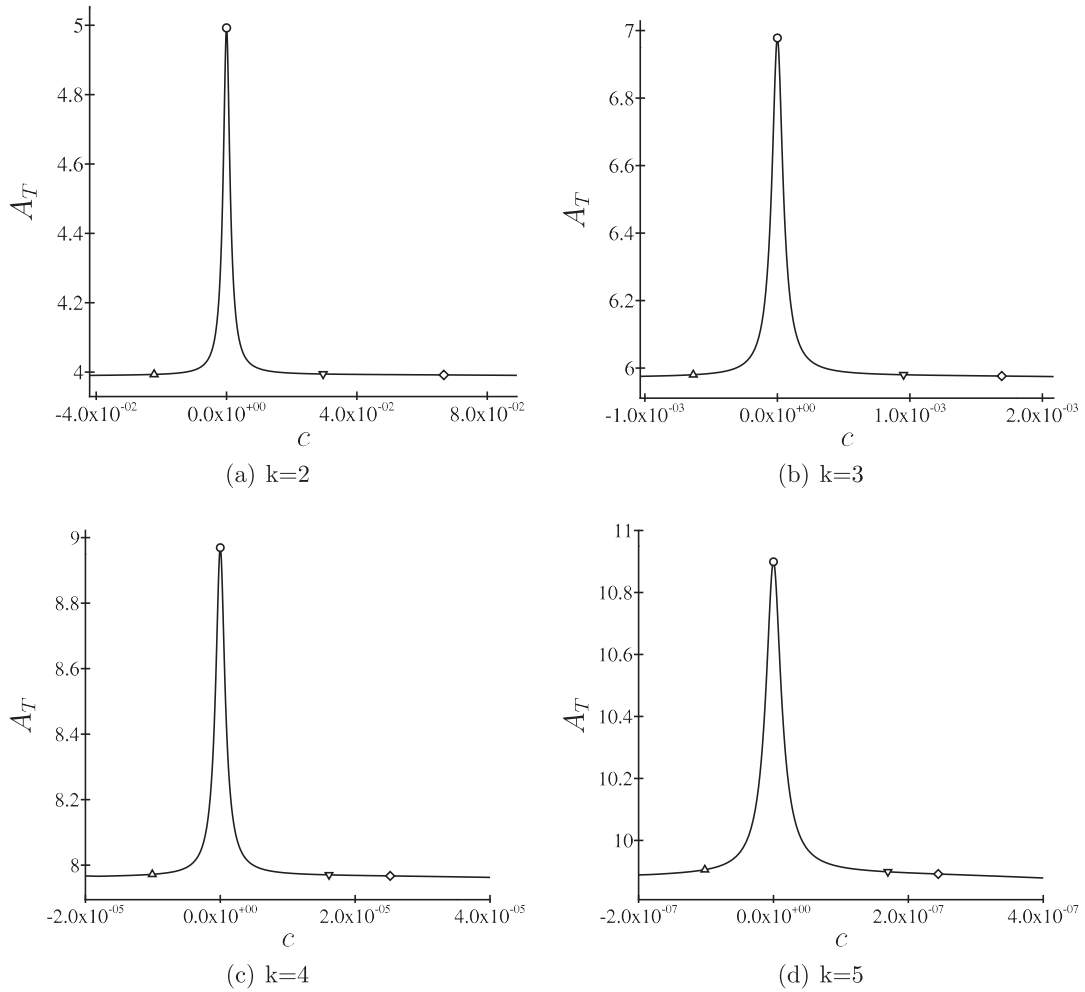


**Fig. 3.** Plots of  $A_T$  against  $c$  when  $k = 2$  (a),  $k = 3$  (b),  $k = 4$  (c), and  $k = 5$  (d).  $A_T$  was obtained using a value of  $\theta_R^\delta = \pi/8$  when  $k = 2$ , a value of  $\theta_R^\delta = \pi/4$  when  $k = 3$ , a value of  $\theta_R^\delta = \pi/3$  when  $k = 4$ , and a value of  $\theta_R^\delta = 2\pi/3$  when  $k = 5$ . Hollow shaped markers denote particular values of  $c$ . Specifically, up-triangle is at  $c = c_-/2$ , circle is at  $c = c_{DG}$ , down-triangle is at  $c = c_{SD}$ , and diamond is at  $c = c_{HU}$ . For all values of  $k$ , a maximal value of  $A_T \approx 2k + 1$  is attained when  $c = c_{DG}$ . Also, for all values of  $k$ ,  $A_T \approx 2k$  when  $c = c_-/2$ ,  $c = c_{SD}$ , and  $c = c_{HU}$ .

temporal discretizations with high-order spatial discretizations, since implicit schemes do not suffer from such a severe time-step restriction. However, the cost of taking an implicit time-step is significantly higher than the cost of taking an explicit time-step, and the complexity of an implicit scheme is significantly greater than that of an explicit scheme. Moreover, it appears that explicit temporal discretizations are better suited to multi-core (low memory-per-core) architectures such as GPUs, which have become increasingly popular in recent years. When performing time-accurate high-order simulations, it therefore remains an open question as to whether explicit or implicit temporal discretizations offer the most efficient solution. The objective of the following section is to investigate how explicit time-step limits vary across the full range of VCJH schemes.

5.2. Theory

The analysis follows directly from that presented in Section 4, and all assumptions are retained. If  $\hat{\mathbf{u}}^\delta$  is a Bloch wave solution of the form described by Eq. (4.11), then Eq. (4.9) can be written as

$$\frac{d\hat{\mathbf{u}}^\delta}{dt} = -\mathbf{I}\mathbf{Q}\hat{\mathbf{u}}^\delta. \tag{5.1}$$

An explicit Runge–Kutta (RK) temporal discretization of Eq. (5.1) leads to an expression of the form

$$\hat{\mathbf{u}}^{\delta(m+1)} = \mathbf{R}\hat{\mathbf{u}}^{\delta(m)}, \tag{5.2}$$

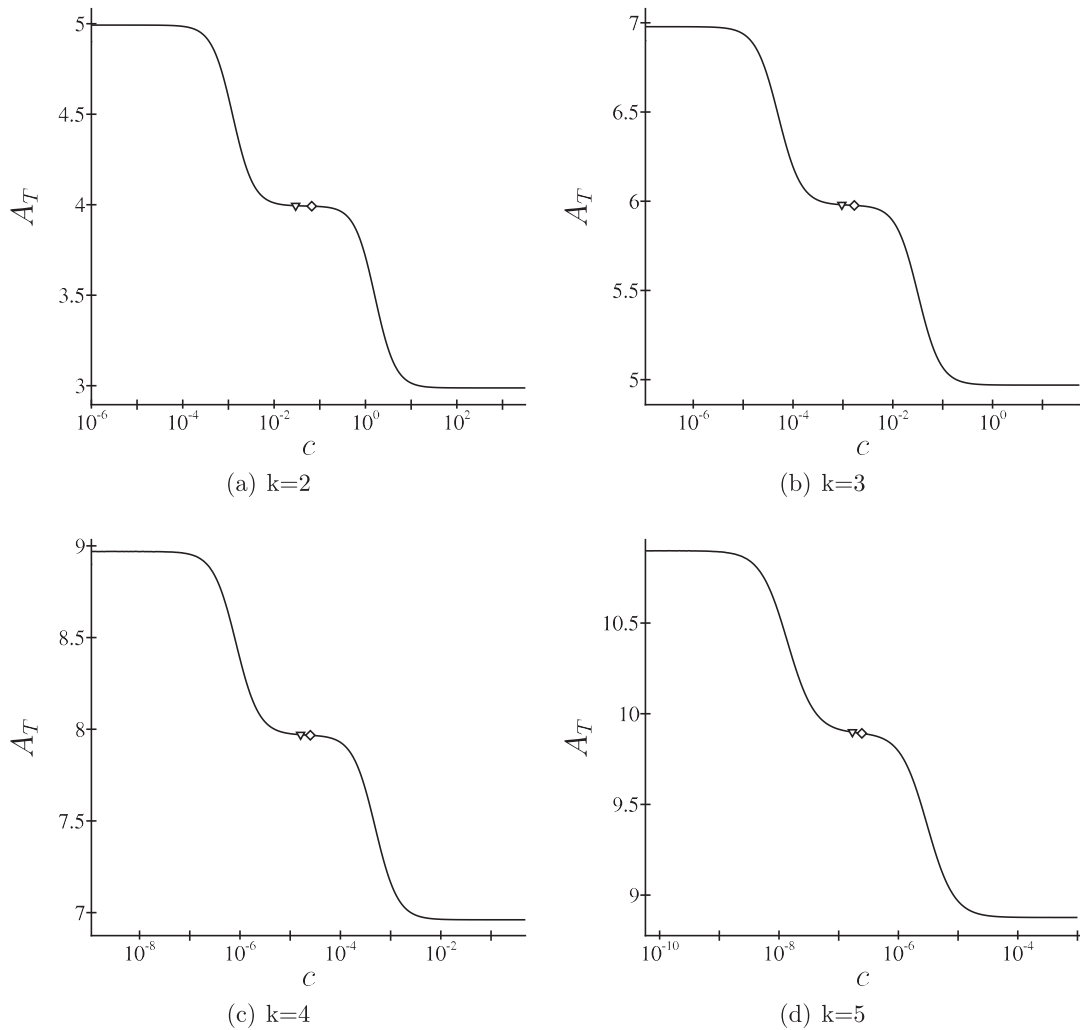


**Fig. 4.** Semi-log plots of  $A_T$  against  $c$  when  $k = 2$  (a),  $k = 3$  (b),  $k = 4$  (c), and  $k = 5$  (d).  $A_T$  was obtained using a value of  $\theta_R^\delta = \pi/8$  when  $k = 2$ , a value of  $\theta_R^\delta = \pi/4$  when  $k = 3$ , a value of  $\theta_R^\delta = \pi/3$  when  $k = 4$ , and a value of  $\theta_R^\delta = 2\pi/3$  when  $k = 5$ . Hollow shaped markers denote particular values of  $c$ . Specifically, down-triangle is at  $c = c_{SD}$ , and diamond is at  $c = c_{HU}$ . For all values of  $k$ ,  $c = c_{SD}$  and  $c = c_{HU}$  sit on a plateau where  $A_T \approx 2k$ . Also, for all values of  $k$ ,  $A_T \approx 2k - 1$  in the limit  $c \rightarrow c_\infty$ .

where  $\hat{\mathbf{u}}^{\delta(m)}$  is the approximate solution at time  $t^{(m)}$ ,  $\hat{\mathbf{u}}^{\delta(m+1)}$  is the approximate solution at time  $t^{(m+1)} = t^{(m)} + \tau$ ,  $\tau$  is the time-step, and  $\mathbf{R}$  is a matrix that depends on  $\tau$ ,  $\mathbf{Q}$ , and the type of RK scheme that is employed. Specifically, for a three-stage third-order RK scheme (henceforth referred to as an RK33 scheme)  $\mathbf{R}$  has the form

$$\mathbf{R} = 1 - I\tau\mathbf{Q} - \frac{(\tau\mathbf{Q})^2}{2!} + I\frac{(\tau\mathbf{Q})^3}{3!}, \tag{5.3}$$

for a four-stage fourth-order RK scheme (henceforth referred to as an RK44 scheme)  $\mathbf{R}$  has the form

$$\mathbf{R} = 1 - I\tau\mathbf{Q} - \frac{(\tau\mathbf{Q})^2}{2!} + I\frac{(\tau\mathbf{Q})^3}{3!} + \frac{(\tau\mathbf{Q})^4}{4!}, \tag{5.4}$$

and for the five-stage fourth-order low-storage RK scheme of Carpenter and Kennedy [20] (henceforth referred to as an RK45 scheme)  $\mathbf{R}$  has the form

$$\mathbf{R} = 1 - I\tau\mathbf{Q} - \frac{(\tau\mathbf{Q})^2}{2!} + I\frac{(\tau\mathbf{Q})^3}{3!} + \frac{(\tau\mathbf{Q})^4}{4!} - I\frac{(\tau\mathbf{Q})^5}{200}. \tag{5.5}$$

In order that the fully discrete scheme described by Eq. (5.2) is stable, the spectral radius of  $\mathbf{R}$  must be less than unity for all  $\mathbf{Q}$ . Hence, for a given FR scheme, the spectral radius of  $\mathbf{R}$  must be less than unity for all baseline wavenumbers  $\bar{\theta}^\delta$  in the range  $\pi \leq \bar{\theta}^\delta \leq \pi$ . The maximum stable time-step  $\tau_{CFL}$  for a given FR scheme is defined as the maximum value of  $\tau$  for which this

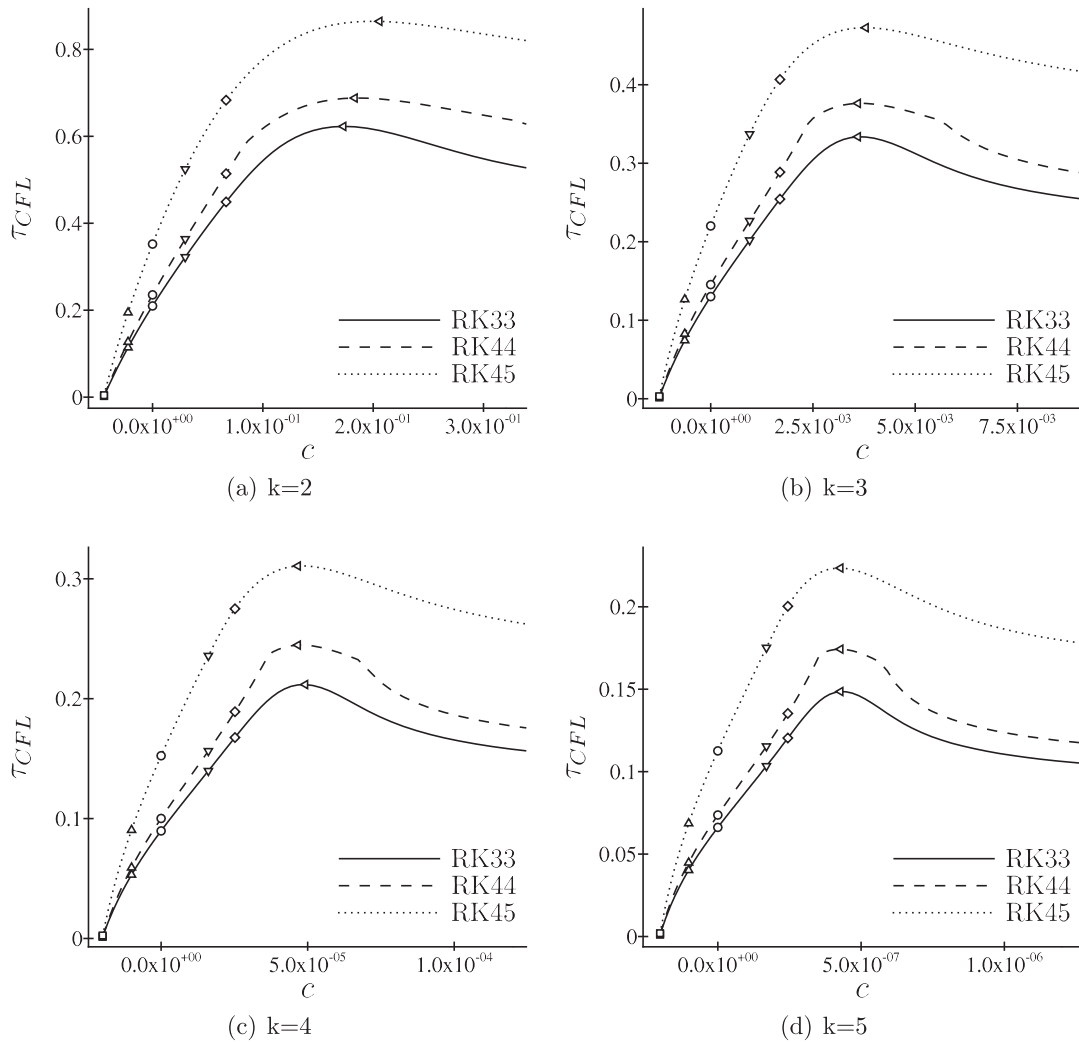


**Fig. 5.** Plots of  $\tau_{CFL}$  against  $c$  when  $k=2$  (a),  $k=3$  (b),  $k=4$  (c), and  $k=5$  (d). Hollow shaped markers denote particular values of  $c$ . Specifically, square is at  $c=c_-$ , up-triangle is at  $c=c_-/2$ , circle is at  $c=c_{DG}$ , down-triangle is at  $c=c_{SD}$ , diamond is at  $c=c_{HU}$ , and left-triangle is at  $c=c_+$ . For all values of  $k$ , and for all RK time-stepping schemes,  $\tau_{CFL}$  is maximized when  $c=c_+$ . Also, for all values of  $k$ , and for all RK time-stepping schemes,  $\tau_{CFL} \rightarrow 0$  as  $c \rightarrow c_-$ .

condition can be satisfied. Note that since the analysis assumes an element width  $h = 1$ , and an advection velocity  $a = 1$ ,  $\tau_{CFL}$  can effectively be considered a non-dimensional maximum time-step (*i.e.* a CFL limit).

### 5.3. Results and discussion

Fig. 5 illustrates how  $\tau_{CFL}$  varies across a range of VCJH schemes for various values of  $k$ , and various types of explicit RK temporal discretization. All VCJH schemes considered had solution points at the Gauss points. The  $c$  axis is on a linear scale so that behavior for negative values of  $c$  can be plotted. Fig. 6 also plots  $\tau_{CFL}$  against  $c$  for various values of  $k$  and various types of explicit RK temporal discretization. However, the  $c$  axis is on a log scale, so that behavior over a larger range of  $c$  can be plotted.

It is clear from Figs. 5 and 6 that  $\tau_{CFL}$  varies non-monotonically with  $c$ . Specifically, for all values of  $k$ , and for all RK temporal discretizations, there exists a value of  $c$  which maximizes  $\tau_{CFL}$ . These values of  $c$ , henceforth denoted  $c_+$ , depend on both  $k$  and the type of RK temporal discretization. Values of  $c_+$  for various values of  $k$  and various RK temporal discretizations are presented in Table 1. For the values of  $k$  and types of RK temporal discretizations considered, use of a VCJH scheme with  $c=c_+$  results in a time-step limit  $\sim 2-3$  times bigger than that for a VCJH scheme with  $c=c_{DG}$ . Finally, it can be noted that for all values of  $k$ , and for all RK temporal discretizations,  $\tau_{CFL} \rightarrow 0$  as  $c \rightarrow c_-$ . Such behavior is expected since VCJH schemes are no longer stable when  $c \leq c_-$ .

Fig. 7 illustrates how, for an RK45 time-integration scheme,  $\tau_{CFL}$  varies with  $A_T$  across the full range of VCJH schemes for various values of  $k$ . All VCJH schemes considered had solution points at the Gauss points. The lines on each plot are

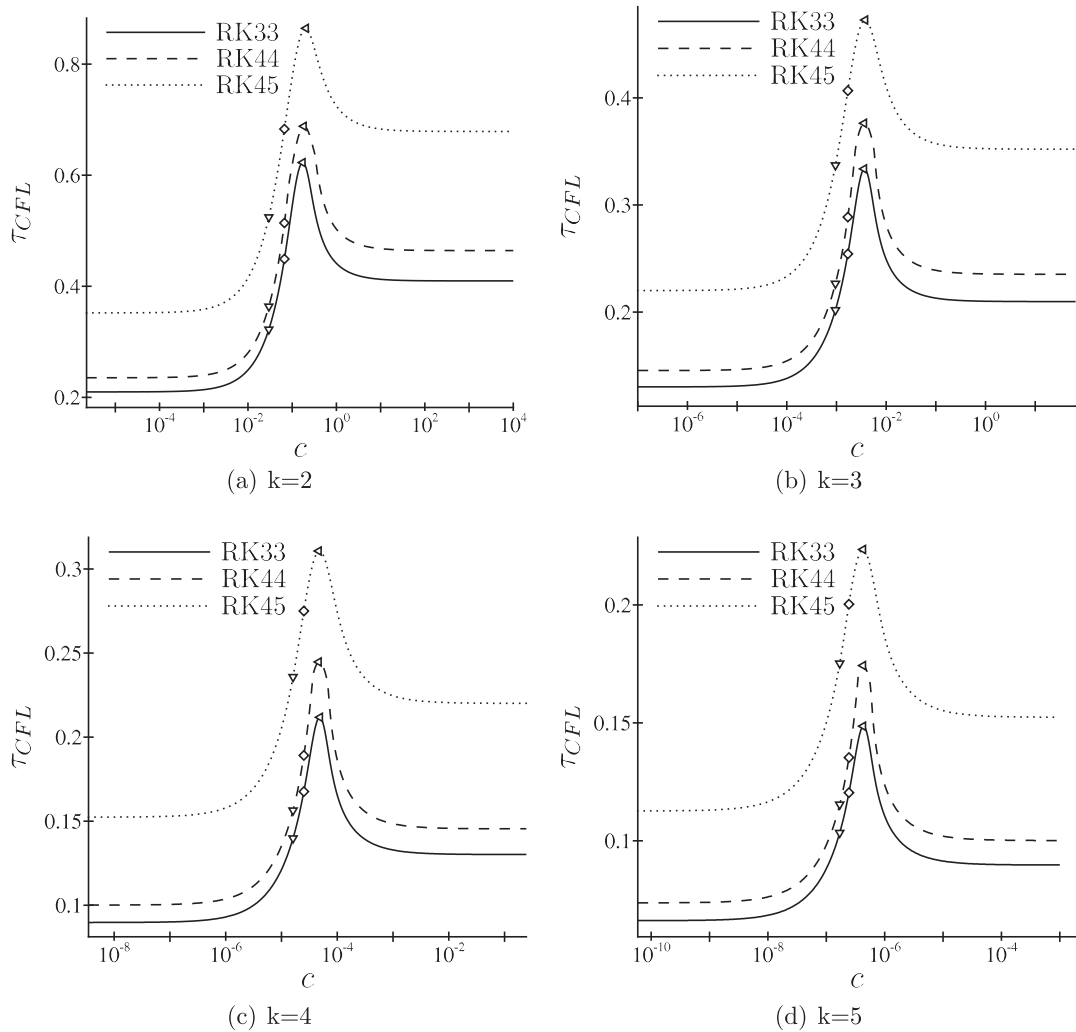


**Fig. 6.** Semi-log plots of  $\tau_{CFL}$  against  $c$  when  $k=2$  (a),  $k=3$  (b),  $k=4$  (c), and  $k=5$  (d). Hollow shaped markers denote particular values of  $c$ . Specifically, down-triangle is at  $c = c_{SD}$ , and diamond is at  $c = c_{HU}$ , and left-triangle is at  $c = c_+$ . For all values of  $k$ , and for all RK time-stepping schemes,  $\tau_{CFL}$  is maximized when  $c = c_+$ .

**Table 1**  
Values of  $c_+$  for various values of  $k$  and various RK temporal discretizations.

		$c_+$
$k=2$	RK33	0.173
	RK44	0.183
	RK45	0.206
$k=3$	RK33	$3.60 \times 10^{-3}$
	RK44	$3.60 \times 10^{-3}$
	RK45	$3.80 \times 10^{-3}$
$k=4$	RK33	$4.92 \times 10^{-5}$
	RK44	$4.67 \times 10^{-5}$
	RK45	$4.67 \times 10^{-5}$
$k=5$	RK33	$4.28 \times 10^{-7}$
	RK44	$4.28 \times 10^{-7}$
	RK45	$4.28 \times 10^{-7}$

essentially parameterized by  $c$ . The full range of  $c$  is spanned in all plots. The solid black arrows indicate the direction of increasing  $c$ . Based on the plots, one should always use a VCJH scheme with  $c_{DG} \leq c \leq c_+$ , since all other schemes can be 'improved upon' (i.e. for schemes with  $c < c_{DG}$  or  $c > c_+$  one can always increase  $\tau_{CFL}$  without decreasing  $A_T$ , or increase  $A_T$  without

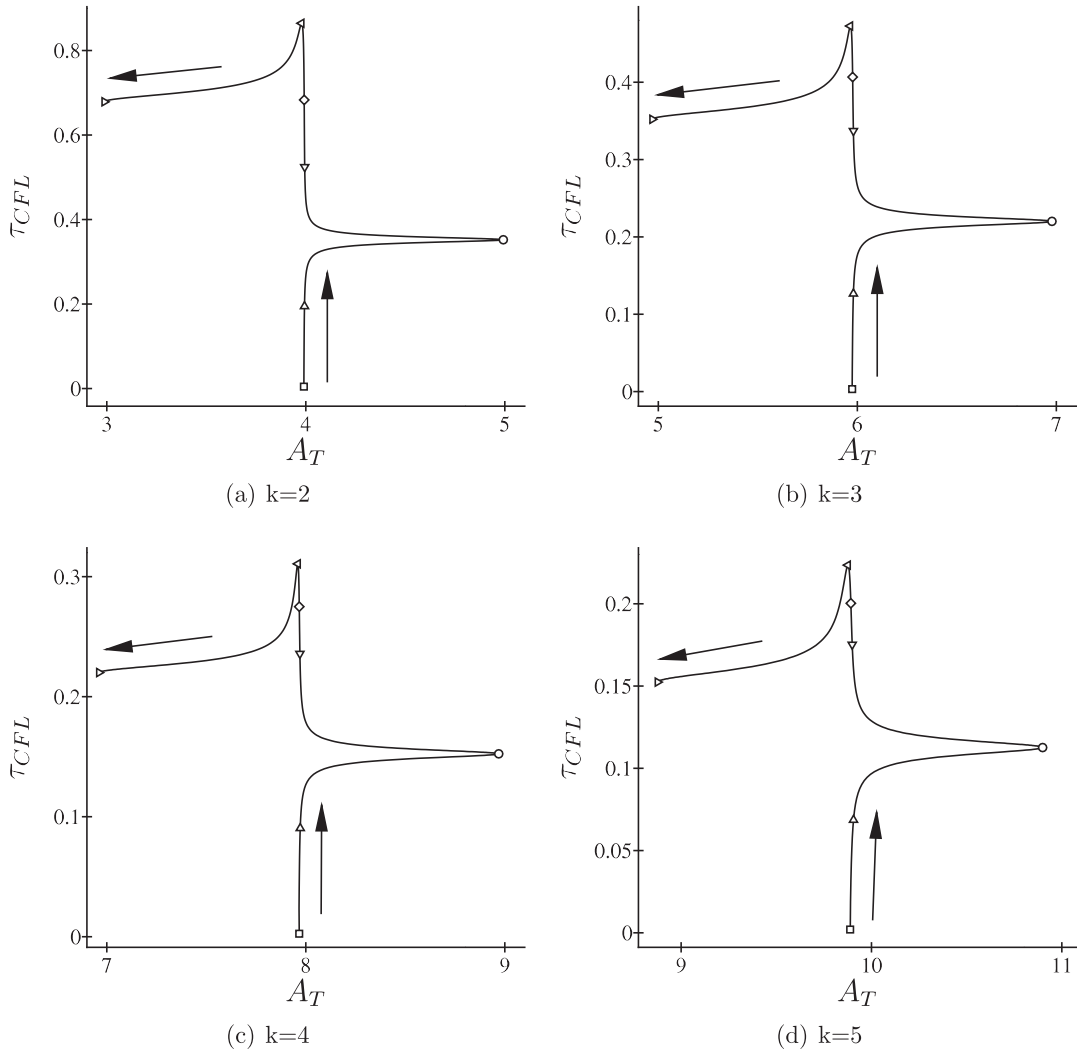


**Fig. 7.** Plots of  $A_T$  against  $\tau_{CFL}$  when  $k = 2$  (a),  $k = 3$  (b),  $k = 4$  (c), and  $k = 5$  (d), for an RK45 scheme. The lines in each plot are essentially parameterized by  $c$ . The hollow symbols mark particular values of  $c$ . Specifically, square is at  $c = c_-$ , up-triangle is at  $c = c_-/2$ , circle is at  $c = c_{DG}$ , down-triangle is at  $c = c_{SD}$ , diamond is at  $c = c_{HU}$ , left-triangle is at  $c = c_+$ , and right-triangle is at  $c = c_\infty$ . The solid black arrows indicate the direction of increasing  $c$ .

decreasing  $\tau_{CFL}$ ). The plots also suggest that VCJH schemes with  $c = c_{DG}$  may be ‘locally optimal’ in some sense, since if  $c_{DG} \leq c \leq c_+$  is near  $c_{DG}$  then moving to a scheme with  $c = c_{DG}$  will significantly increase (and indeed maximize)  $A_T$  for only a small decrement in  $\tau_{CFL}$ . Similarly, VCJH schemes with  $c = c_+$  may also be ‘locally optimal’ in some sense, since if  $c_{DG} \leq c \leq c_+$  is near  $c_+$  then moving to a scheme with  $c = c_+$  will significantly increase (and indeed maximize)  $\tau_{CFL}$  for only a small decrement in  $A_T$ .

## 6. One-dimensional linear numerical experiments

### 6.1. Overview

Several 1D linear numerical experiments were undertaken in order to verify results of the 1D von Neumann analysis presented above. The first set of experiments were designed to verify the theoretical orders of accuracy  $A_T$  (of dispersion and dissipation errors) associated with various VCJH schemes. The second set of experiments were designed to verify the theoretical time-step limits  $\tau_{CFL}$  associated with various VCJH schemes.

### 6.2. Order of accuracy studies

#### 6.2.1. Setup

The experiments undertaken were a variant of those employed by Hu and Atkins [21] to assess the order of accuracy associated with dispersion and dissipation properties of a DG scheme. Specifically, fully upwind VCJH semi-discretizations with

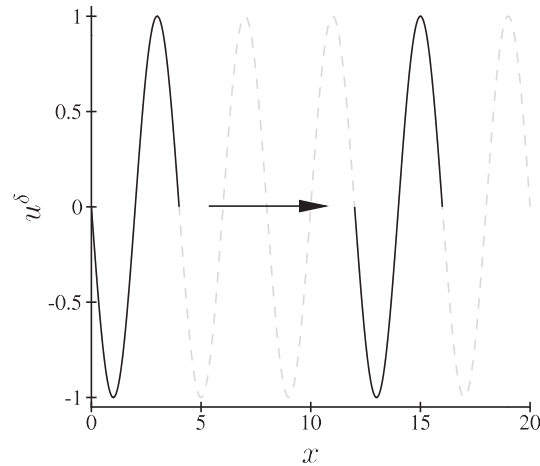


**Fig. 8.** Plot of the solution at  $t = 4L$  where  $L$  is an integer such that  $u^\delta(x, 4L) = u^\delta(x, 4L - 4)$  (dashed gray line). The solution was obtained using a VCJH scheme with  $c = c_{DG}$ ,  $k = 3$ , and  $h = 0.25$ . A section of the solution within  $0 \leq x \leq 4$  is marked with a solid line, as is a section of the solution three wavelengths downstream within  $12 \leq x \leq 16$ .  $E_N$  is defined as the continuous L2 norm of the difference between the solutions within these two regions. The solid black arrow indicates the direction in which the wave is propagating.

$k = 3$ , and solution points at Gauss points, were used to solve Eq. (4.1) in a domain  $\Omega = \{x | 0 < x < 20\}$ , which was meshed with a grid of equisized line segments. All experiments were initiated with a collocation projection of the exact initial condition  $u(x, 0) = 0$ . At  $x = 0$  the time-dependent boundary condition  $u^\delta(0, t) = \sin(\pi t/2)$  was prescribed, and at  $x = 20$  no boundary condition was prescribed (or indeed required) since the interfaces fluxes were fully upwind. In all experiments the equations were discretized in time using an explicit RK45 time integration scheme, and advanced until a left-to-right traveling wave formed within the entirety of  $\Omega$ . Specifically, such a traveling wave was deemed to have formed when  $t = 4L$ , with  $L$  an integer large enough such that  $u^\delta(x, 4L) = u^\delta(x, 4L - 4)$ .

6.2.2. Results and discussion

Experiments were undertaken using VCJH schemes with  $c = c_{DG}$ ,  $c = c_{SD}$ ,  $c = c_{HU}$ , and  $c = c_+$ . For each VCJH scheme grids of 20, 40, 80 and 160 elements were employed, with element lengths of  $h = 1$ ,  $h = 0.5$ ,  $h = 0.25$ , and  $h = 0.125$  respectively. The time-step was chosen small enough such that in all experiments the temporal error was negligible.

A numerical error  $E_N$  was obtained by taking a snapshot of the solution at  $t = 4L$ , and evaluating a continuous L2 norm of the difference between the solution within  $0 \leq x \leq 4$  and the solution three wavelengths downstream within  $12 \leq x \leq 16$ , (see Fig. 8). This procedure isolates only dispersion and dissipation errors associated with the VCJH spatial operator, as opposed to any errors associated with initial or boundary conditions. Note that the continuous L2 norm was evaluated exactly using a Gaussian quadrature rule (of sufficient strength). This is possible since  $E_N$  is based on the error between two polynomials approximations.

Fig. 9 plots element length  $h$  against error  $E_N$  on a log-log scale for the various VCJH schemes. The hollow symbols correspond to measured data points. The lines on the plots are (linear) least-squares fits of data associated with each distinct VCJH scheme. The slope of each line gives an estimate of the order  $A_N$  with which the error  $E_N$  converges for each VCJH scheme. For a VCJH scheme with  $c = c_{DG}$  a super accurate value of  $A_N = 6.96$  was obtained, for a VCJH scheme with  $c = c_{SD}$  a super accurate value of  $A_N = 5.97$  was obtained, for a VCJH scheme with  $c = c_{HU}$  a super accurate value of  $A_N = 5.96$  was obtained, and for a VCJH scheme with  $c = c_+$  a super accurate value of  $A_N = 5.94$  was obtained. These numerical results agree with those obtained using 1D von Neumann analysis, which for VCJH schemes with  $k = 3$  where:  $A_T \approx 7$  when  $c = c_{DG}$ , and  $A_T \approx 6$  when  $c = c_{SD}$ ,  $c = c_{HU}$ , and  $c = c_+$ .

6.3. Time-step limit studies

6.3.1. Setup

Fully upwind VCJH semi-discretizations with  $k = 3$ , and solution points at Gauss points, were used to solve Eq. (4.1) in a domain  $\Omega = \{x | -20 < x < 20\}$ , which was meshed with a grid of equisized line segments. All experiments were initiated with a collocation projection of the following exact initial condition

$$u(x, 0) = e^{-x^2/10}, \tag{6.1}$$

and periodic boundary conditions were applied at  $x = \pm 20$ . In all experiments the equations were discretized in time using an explicit RK45 time integration scheme, and advanced until  $t = 1600$ .

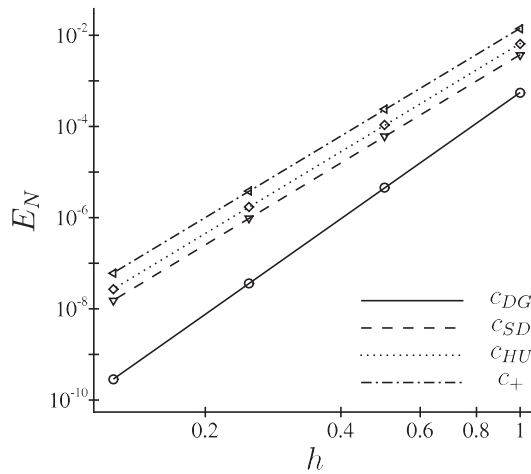


**Fig. 9.** Log-log plots of error  $E_N$  against element length  $h$  for various VCJH schemes when  $k = 3$ . Circles mark data points for schemes with  $c = c_{DG}$ , down-triangles mark data points for schemes with  $c = c_{SD}$ , diamonds mark data points for schemes with  $c = c_{HU}$ , and left-triangles mark data points for schemes with  $c = c_+$ . The lines are (linear) least-squares fits through data associated with each distinct VCJH scheme.

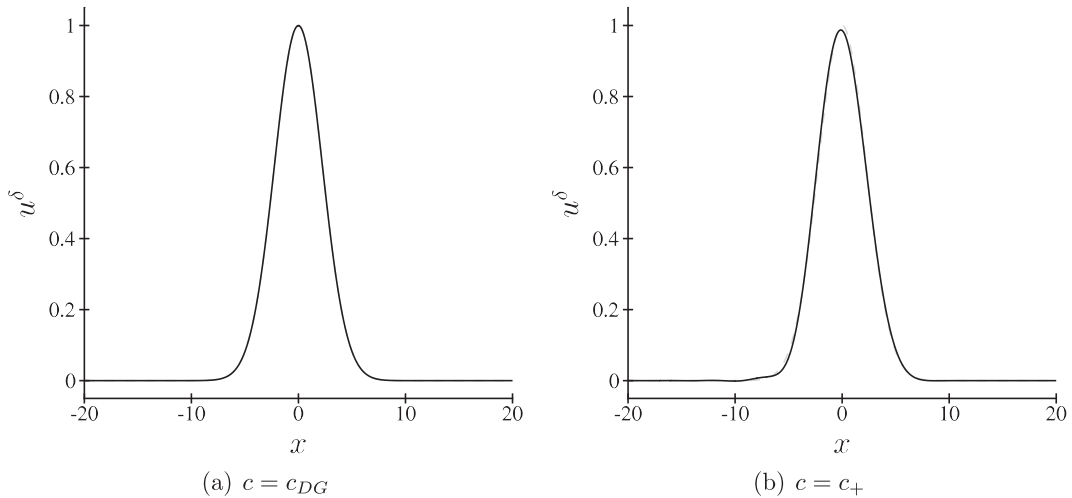


**Fig. 10.** Plots of the solution at  $t = 1600$  for VCJH schemes with  $c = c_{DG}$  (a) and  $c = c_+$  (b) when running at a CFL number 1% below the relevant theoretical CFL limit (based on 1D von Neumann analysis). The initial condition is shown with a dashed gray line in each plot.

6.3.2. Results and discussion

Experiments were undertaken using VCJH schemes with  $c = c_{DG}$ ,  $c = c_{SD}$ ,  $c = c_{HU}$ , and  $c = c_+$  on grids of 40 elements (with an element length of  $h = 1$ ). In all cases, experiments were run at a CFL number either 1% below or 1% above the relevant theoretical CFL limit  $\tau_{CFL}$  (based on 1D von Neumann analysis). Specifically, for the VCJH scheme with  $c = c_{DG}$  time-steps of  $0.2201 \times (1 \pm 0.01)$  were used, for the VCJH scheme with  $c = c_{SD}$  time-steps of  $0.3371 \times (1 \pm 0.01)$  were used, for the VCJH scheme with  $c = c_{HU}$  time-steps of  $0.4067 \times (1 \pm 0.01)$  were used, and for the VCJH scheme with  $c = c_+$  time-steps of  $0.4727 \times (1 \pm 0.01)$  were used.

When using a time-step 1% below the theoretical CFL limit each experiment remained stable until it was stopped at  $t = 1600$ . Plots of the final solutions for VCJH schemes with  $c = c_{DG}$  and  $c = c_+$  are shown in Fig. 10. However, when using a time-step 1% above the theoretical CFL limit each experiment quickly became unstable. The numerical results therefore support the findings of the 1D von Neumann analysis.

7. Two-dimensional non-linear numerical experiments

7.1. Overview

Several 2D non-linear numerical experiments were undertaken to ascertain whether results of the 1D von Neumann analysis presented above extend to real world problems of practical interest. The first set of experiments were designed

to measure the orders of accuracy (of dispersion and dissipation errors) associated with various VCJH schemes. The second set of experiments were designed to measure explicit time-step limits associated with various VCJH schemes.

## 7.2. Order of accuracy studies

### 7.2.1. Setup

The 2D time-dependent Euler equations governing flow of an inviscid compressible fluid with density  $\rho = \rho(x, y, t)$ ,  $x$ -velocity  $v_x = v_x(x, y, t)$ ,  $y$ -velocity  $v_y = v_y(x, y, t)$ , and pressure  $p = p(x, y, t)$  can be written in conservative form as follows

$$\frac{\partial \mathbf{U}}{\partial t} + \frac{\partial \mathbf{F}}{\partial x} + \frac{\partial \mathbf{G}}{\partial y} = 0, \quad (7.1)$$

where

$$\mathbf{U} = \begin{pmatrix} \rho \\ m_x \\ m_y \\ E \end{pmatrix}, \quad \mathbf{F} = \begin{pmatrix} m_x \\ p + m_x v_x \\ m_x v_y \\ v_x(E + p) \end{pmatrix}, \quad \mathbf{G} = \begin{pmatrix} m_y \\ m_y v_x \\ p + m_y v_y \\ v_y(E + p) \end{pmatrix}, \quad (7.2)$$

$$m_x = \rho v_x, \quad (7.3)$$

$$m_y = \rho v_y, \quad (7.4)$$

$$E = \frac{p}{(\gamma - 1)} + \frac{1}{2} \rho (v_x^2 + v_y^2), \quad (7.5)$$

$x$  and  $y$  are orthogonal spatial coordinates,  $t$  is time, and  $\gamma = 1.4$ .

VCJH schemes were used to solve Eq. (7.1) in a domain  $\Omega_{2D} = \{x, y | -20 < x < 20, -20 < y < 20\}$ , which was meshed with a structured grid of square elements. In each element Eq. (7.1) was discretized spatially using a tensor product extension [2] of the 1D VCJH schemes described in Section 3. Specifically, tensor product extensions of 1D VCJH schemes with  $k = 3$  were employed in each element. At element interfaces Rusanov type numerical fluxes [22] (also referred to as a local Lax-Fredrichs fluxes) were calculated in order to couple the elements. Solution points were located at the Gauss points (in each direction of the tensor product) so as to minimize aliasing errors, which manifest if non-linear solutions are marginally resolved by a FR scheme [23].

The initial condition for all experiments was a collocation projection at the solution points of the following isentropic vortex in a free-stream flow (in the positive  $y$  direction)

$$\rho(x, y, 0) = \left( 1 - \frac{\Gamma^2 M^2 (\gamma - 1) e^{2f}}{8\pi^2} \right)^{\frac{1}{\gamma-1}}, \quad (7.6)$$

$$v_x(x, y, 0) = \frac{\Gamma y e^f}{2\pi R}, \quad (7.7)$$

$$v_y(x, y, 0) = 1 + \frac{\Gamma x e^f}{2\pi R}, \quad (7.8)$$

$$p(x, y, 0) = \frac{1}{\gamma M^2} \left( 1 - \frac{\Gamma^2 M^2 (\gamma - 1) e^{2f}}{8\pi^2} \right)^{\frac{\gamma}{\gamma-1}}, \quad (7.9)$$

where  $f = f(x, y)$  is defined as

$$f = \frac{1 - x^2 - y^2}{2R^2}, \quad (7.10)$$

$R$  is the radius of the vortex,  $\Gamma$  is the strength of the vortex, and  $M$  is the free-stream Mach number. In all experiments, values of  $R = 1.5$ ,  $\Gamma = 13.5$ , and  $M = 0.4$  were used. A collocation projection at the solution points of the initial density  $\rho(x, y, 0)$  on a grid of  $120 \times 120$  square elements is shown in Fig. 11.

In all experiments free-stream values were applied at boundaries of constant  $x$  as follows

$$\begin{aligned} \rho(-20, y, t) = \rho(20, y, t) = 1, \quad u(-20, y, t) = u(20, y, t) = 0, \\ v(-20, y, t) = v(20, y, t) = 1, \quad p(-20, y, t) = p(20, y, t) = \left( \frac{1}{\gamma M^2} \right), \end{aligned} \quad (7.11)$$

and periodic boundary conditions were applied in the  $y$  direction as follows

$$\begin{aligned} \rho(x, -20, t) = \rho(x, 20, t), \quad u(x, -20, t) = u(x, 20, t), \\ v(x, -20, t) = v(x, 20, t), \quad p(x, -20, t) = p(x, 20, t). \end{aligned} \quad (7.12)$$

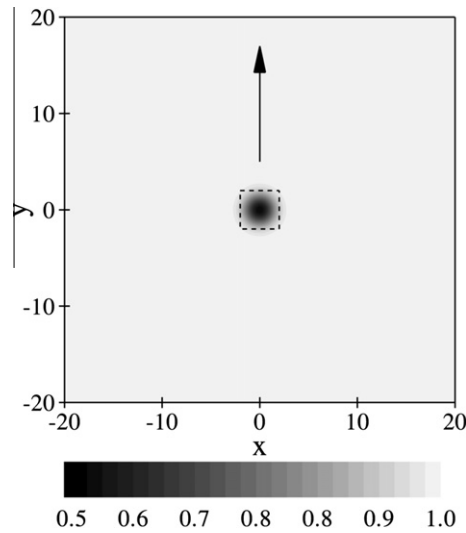


**Fig. 11.** Collocation projection (at the solution points) of the initial density  $\rho(x,y,0)$  on a mesh of  $120 \times 120$  square elements. The dashed box surrounds the area in which the continuous L2 error  $E_{N2D}$  is calculated at  $t = 0$ . The solid arrow indicates the direction in which the vortex will be transported by the free-stream flow.

Strictly, such conditions result in modelling an infinite array of coupled vortices. However, since  $R$  is significantly less than the domain half-width, and since the vortex described by Eqs. (7.6)–(7.9) decays exponentially from its center, the initial isentropic vortex has a negligible impact on the free-stream at boundaries of  $\Omega_{2D}$ . Consequently, application of Eqs. 7.11 and 7.12 effectively result in modelling a single unbounded vortex in an infinite domain.

In all experiments the equations were discretized in time using an explicit RK45 time integration scheme, and advanced until  $t = 1800$ .

### 7.2.2. Results and discussion

Experiments were undertaken using VCJH schemes with  $c = c_{DG}$ ,  $c = c_{SD}$ ,  $c = c_{HU}$ , and  $c = c_+$ . For each distinct VCJH scheme, experiments were performed on grids of  $120 \times 120$ ,  $140 \times 140$ ,  $160 \times 160$ , and  $180 \times 180$  elements, with element side lengths of  $h_{2D} = 1/3$ ,  $h_{2D} = 2/7$ ,  $h_{2D} = 1/4$ , and  $h_{2D} = 2/9$  respectively. The time-step was chosen small enough such that in all experiments the temporal error was negligible.

Since the isentropic vortex is effectively unbounded a well known analytical solution exists for the evolution of Eqs. (7.6)–(7.9) [24] within  $\Omega_{2D}$ . Specifically, the true solution is simply a translation of the exact initial condition in the positive  $y$  direction at the free-stream velocity, (with the caveat that the solution moves back into the bottom of  $\Omega_{2D}$ , at  $y = -20$ , as it leaves from the top, at  $y = 20$ , due to the periodic boundary conditions). A numerical error  $E_{N2D}$  was obtained by taking the continuous L2 norm of the error between the true analytical solution for the density and the approximate numerical solution for the density within a square box of side length four, which is aligned with the coordinate axes, and centered over the true analytic density minimum (see Fig. 11). The L2 norm was calculated using a high-strength Gaussian quadrature rule, such that errors from evaluating the integral were negligible relative to the actual error in the density.

For each VCJH scheme, and on each of the four grids, the evolution of  $E_{N2D}$  with time  $t$  was recorded. The errors  $E_{N2D}$  were subsequently used to calculate the evolution (with time  $t$ ) of an order of accuracy  $A_{N2D}$  for each VCJH scheme. Specifically, for a given VCJH scheme, and at a given time,  $A_{N2D}$  was calculated by plotting  $E_{N2D}$  against  $h_{2D}$  on a log-log scale, and calculating the slope of a (linear) least-squares fit through the data points. Fig. 12 plots values of  $A_{N2D}$  against time  $t$  for the each VCJH schemes. Fig. 13 plots errors  $E_{N2D}$  against  $h_{2D}$  on a log-log scale at the final time  $t = 1800$  for each VCJH scheme. Finally, Fig. 14 plots the spatial distribution of the density error at the final time  $t = 1800$  for each VCJH scheme on a grid of  $120 \times 120$  elements. Note that the errors are plotted in a square box of side length four, which is aligned with the coordinate axes, and centered over the true analytic density minimum, (this is the same region within which  $E_{N2D}$  is calculated).

It is clear from Fig. 12 that  $A_{N2D} \approx 4$  when  $t = 0$  for all VCJH schemes. This is expected, since at  $t = 0$  the errors are entirely due to projection of the exact initial condition onto a piecewise polynomial space of degree three in each element. However, as time advances, values of  $A_{N2D}$  associated with each VCJH scheme increase (the solutions begin to exhibit super accuracy). Specifically, for the VCJH scheme with  $c = c_{DG}$ ,  $A_{N2D} \approx 7$  for large  $t$ , and for VCJH schemes with  $c = c_{SD}$ ,  $c = c_{HU}$ , and  $c = c_+$ ,  $A_{N2D} \approx 6$  for large  $t$ . At large times  $E_{N2D}$  is dominated by dispersion and dissipation errors associated with the VCJH spatial operator, as opposed to initial projection errors. Consequently, the numerical results appear to be in agreement with the results obtained using 1D von Neumann analysis, which for VCJH schemes with  $k = 3$  were:  $A_T \approx 7$  when  $c = c_{DG}$ , and  $A_T \approx 6$  when  $c = c_{SD}$ ,  $c = c_{HU}$ , and  $c = c_+$ .

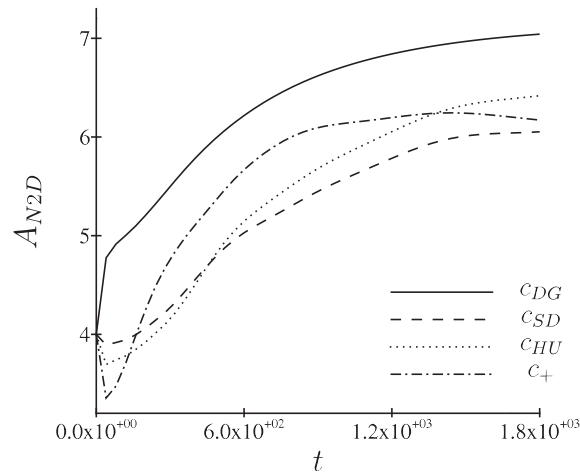


Fig. 12. Plot of the evolution of order of accuracy  $A_{N2D}$  with time  $t$  for various VCJH schemes with  $k = 3$ .

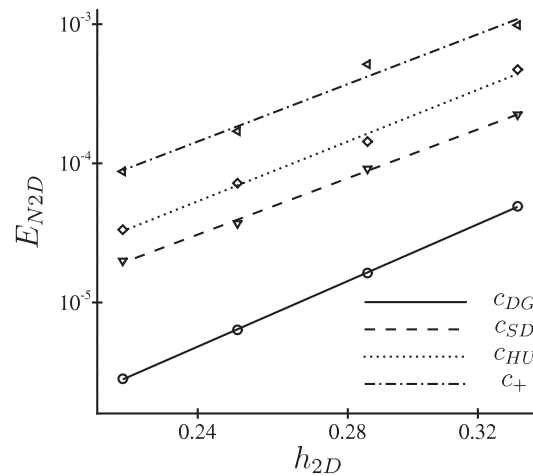


Fig. 13. Log-log plots of error  $E_{N2D}$  against element side length  $h_{2D}$  at  $t = 1800$  for various VCJH schemes with  $k = 3$ . Circles mark data points for schemes with  $c = c_{DG}$ , down-triangles mark data points for schemes with  $c = c_{SD}$ , diamonds mark data points for schemes with  $c = c_{HU}$ , and left-triangles mark data points for schemes with  $c = c_+$ . The lines are (linear) least-squares fits through data for each VCJH scheme.

### 7.3. Time-step limit studies

#### 7.3.1. Setup

The setup was identical to that described in Section 7.2.1, except the solution was only advanced in time until  $t = 20$ .

#### 7.3.2. Results and discussion

Experiments were undertaken using VCJH schemes with  $c = c_{DG}$ ,  $c = c_{SD}$ ,  $c = c_{HU}$ , and  $c = c_+$  on grids of  $120 \times 120$  elements (with an element side length of  $h_{2D} = 1/3$ ).

An iterative strategy was employed to empirically determine the maximum stable time-step for each VCJH scheme. Specifically, a time-step was deemed to be stable if the solution at the final time  $t = 20$  remained bounded. The maximum stable time-steps for VCJH schemes with  $c = c_{DG}$ ,  $c = c_{SD}$ ,  $c = c_{HU}$ , and  $c = c_+$  were measured to be 0.0101, 0.0143, 0.0165 and 0.0169 respectively, which correspond to CFL limits of 0.152, 0.216, 0.250, and 0.255 respectively (using a characteristic length of  $1/3$  and a characteristic velocity of 5.03, which is the maximum value of the sum between the velocity magnitude and the sound speed within the domain  $\Omega_{2D}$ ). These CFL limits are of the same order of magnitude as those predicted by 1D von Neumann analysis (see Fig. 5(b) and Fig. 6(b)). Moreover, the measured CFL limits increase as  $c$  is increased from  $c = c_{DG}$  to  $c = c_+$ , following the trend predicted using 1D von Neumann analysis. However, the measured CFL limit only increases by a factor of 1.67 going from  $c = c_{DG}$  to  $c = c_+$ , whereas the corresponding CFL limits predicted using 1D von Neumann analysis increase by a factor of 2.15.

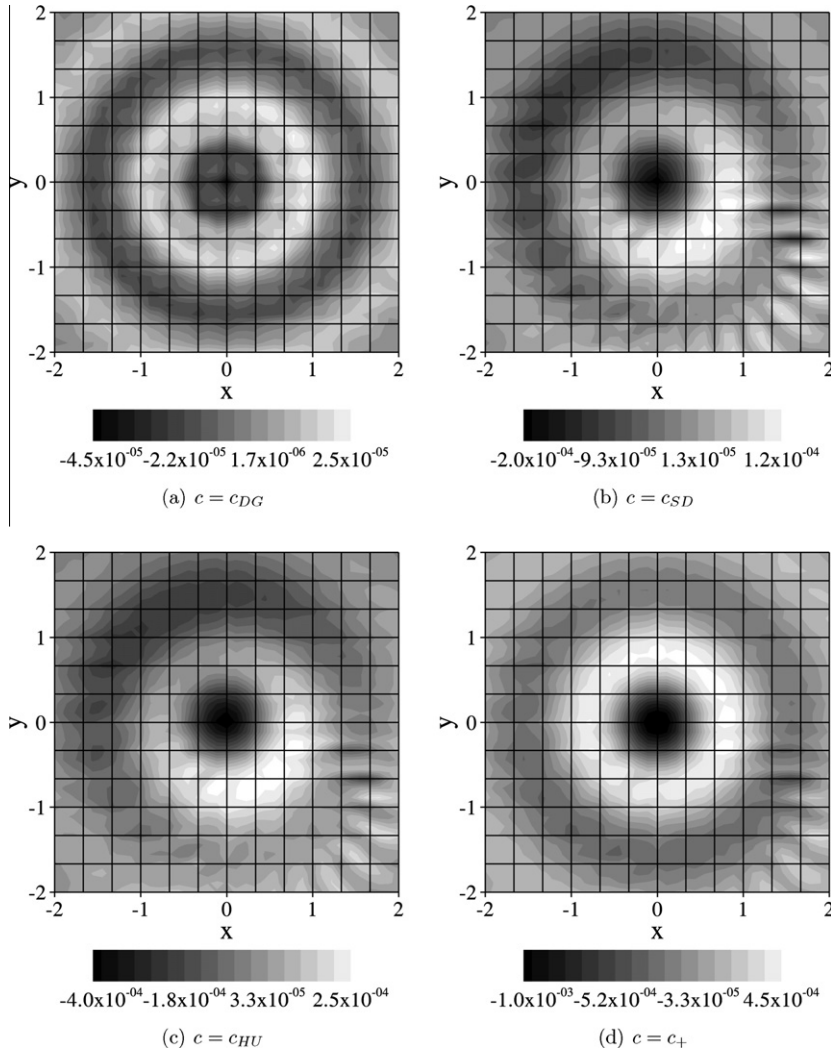


**Fig. 14.** Spatial distribution of density error at  $t = 1800$  for each VCJH scheme on a grid of  $120 \times 120$  elements. Note that the errors are plotted in a square box of side length four, which is aligned with the coordinate axes, and centered over the true analytic density minimum, (this is the same region within which  $E_{N2D}$  is calculated).

### 8. Conclusion

In this study 1D von Neumann analysis was employed to elucidate how various important properties vary across the full range of VCJH type FR schemes. The main findings can be summarized as follows. Firstly, VCJH schemes with values of  $c$  near  $c_-$  or  $c_\infty$  admit undamped high-wavenumber Bloch wave solutions with erroneous dispersion relations. Consequently, such schemes are unfavorable, and should be avoided. Secondly, the dispersion relation for a VCJH scheme with  $c = c_{SD}$  follows the true dispersion relation (at least for linear advection) over an approximately maximal range of wavenumbers. Thirdly, the order of accuracy  $A_T$  associated with dispersion and dissipation errors varies non-monotonically with  $c$  (i.e. non-monotonically across the range of VCJH schemes). Specifically, for all values of  $k$  considered, a maximal value of  $A_T \approx 2k + 1$  is attained when  $c = c_{DG}$ , and there exists a plateau of  $A_T \approx 2k$  on which VCJH schemes with  $c = c_{SD}$  and  $c = c_{HU}$  both reside. Fourthly, the CFL limit  $\tau_{CFL}$  varies non-monotonically with  $c$  (i.e. non-monotonically across the range of VCJH schemes). Specifically, for all values of  $k$  and for all RK temporal discretizations, there exists a value of  $c$ , denoted  $c_+$ , which maximizes  $\tau_{CFL}$ . These values of  $c_+$  have been identified, and are presented in Table 1. Finally, VCJH schemes with  $c = c_{DG}$  and  $c = c_+$  may be ‘locally optimal’ in some sense, since if  $c$  is near  $c_{DG}$  then moving to a scheme with  $c = c_{DG}$  will significantly increase (and indeed maximize)  $A_T$  for only a small decrement in  $\tau_{CFL}$ , and similarly if  $c$  is near  $c_+$ , then moving to a scheme with  $c = c_+$  will significantly increase (and indeed maximize)  $\tau_{CFL}$  for only a small decrement in  $A_T$ .

Results of the 1D von Neumann analysis were found to be in excellent agreement with results of 1D linear numerical experiments, and in good agreement with results of 2D non-linear numerical experiments. Consequently, it is hoped that

the theoretical results will extend to various real world problems of practical interest. Future studies should confirm that this is the case. Additionally, future studies should investigate how other properties vary across the full range of VCJH schemes, including error magnitude (as opposed to order of accuracy), and non-linear stability (previous studies [8] suggest increasing  $c$  beyond  $c = c_{DG}$  suppresses aliasing driven instabilities, which manifest if a non-linear solution is marginally resolved by a FR scheme [23]).

## Acknowledgements

The authors would like to thank the National Science Foundation (grants 0708071 and 0915006), the Air Force Office of Scientific Research (grants FA9550-07-1-0195 and FA9550-10-1-0418), the Natural Sciences and Engineering Research Council of Canada and the Fonds de Recherche sur la Nature et les Technologies du Québec for supporting this work. The authors would also like to thank David Williams and Kui Ou for useful discussions, and Philipp Birken for carefully reviewing a first draft of the paper.

## References

- [1] P.E. Vincent, A. Jameson, Facilitating the adoption of unstructured high-order methods amongst a wider community of fluid dynamicists, *Math. Mod. Nat. Phenom.* 6 (2011) 97.
- [2] H.T. Huynh, A flux reconstruction approach to high-order schemes including discontinuous Galerkin methods, *AIAA Paper 2007-4079*, 2007.
- [3] Z.J. Wang, H. Gao, A unifying lifting collocation penalty formulation including the discontinuous Galerkin, spectral volume/difference methods for conservation laws on mixed grids, *J. Comput. Phys.* 228 (2009) 8161.
- [4] J.S. Hesthaven, T. Warburton, *Nodal Discontinuous Galerkin methods – Algorithms, Analysis, and Applications*, Springer, 2008.
- [5] D.A. Kopriva, J.H. Kolas, A conservative staggered-grid Chebyshev multidomain method for compressible flows, *J. Comput. Phys.* 125 (1996) 244.
- [6] Y. Liu, M. Vinokur, Z.J. Wang, Spectral difference method for unstructured grids I: Basic formulation, *J. Comput. Phys.* 216 (2006) 780.
- [7] H.T. Huynh, A reconstruction approach to high-order schemes including discontinuous Galerkin for diffusion, *AIAA Paper 2009-403*, 2009.
- [8] P.E. Vincent, P. Castonguay, A. Jameson, A new class of high-order energy stable flux reconstruction schemes, *J. Sci. Comput.* 47 (2011) 50.
- [9] P.L. Roe, Approximate Riemann solvers, parameter vectors, and difference schemes, *J. Comput. Phys.* 43 (1981) 357.
- [10] A. Jameson, A proof of the stability of the spectral difference method for all orders of accuracy, *J. Sci. Comput.* 45 (2010) 348.
- [11] K. Van den Abeele, T. Broeckhoven, C. Lacor, Dispersion and dissipation properties of the 1D spectral volume method and application to a  $p$ -multigrid algorithm, *J. Comput. Phys.* 224 (2007) 616.
- [12] K. Van den Abeele, *Development of High-order Accurate Schemes for Unstructured Grids*, Ph.D. thesis, Vrije Universiteit Brussel, 2009.
- [13] F.Q. Hu, M.Y. Hussaini, P. Rasetarinera, An analysis of the discontinuous Galerkin method for wave propagation problems, *J. Comput. Phys.* 151 (1999) 921.
- [14] S. Sherwin, Dispersion analysis of the continuous and discontinuous Galerkin formulation, *Lect. Notes. Comput. Sci.* 11 (2000) 425.
- [15] M. Ainsworth, Discrete dispersion relation for hp-version finite element approximation at high wave number, *SIAM J. Numer. Anal.* 42 (2005) 553.
- [16] M. Ainsworth, P. Monk, W. Muniz, Dispersive and dissipative properties of discontinuous Galerkin finite element methods for the second-order wave equation, *J. Sci. Comput.* 27 (2006) 5.
- [17] H. Ibach, H. Luth, *Solid State Physics: An Introduction to Principles of Materials Science*, fourth ed., Springer, 2009.
- [18] H.L. Atkins, B. Helenbrook, Super-convergence of discontinuous Galerkin method applied to the Navier–Stokes equations, *AIAA Paper 2009-3787*, 2009.
- [19] J.S. Hesthaven, D. Gottlieb, Stable spectral methods for conservation laws on triangles with unstructured grids, *Comput. Method Appl. M* 175 (1999) 361.
- [20] M.H. Carpenter, C. Kennedy, Fourth-order 2N-Storage Runge–Kutta Schemes, Technical Report TM 109112, NASA, NASA Langley Research Center, 1994.
- [21] F.Q. Hu, H.L. Atkins, Eigensolution analysis of the discontinuous Galerkin method with nonuniform grids: I. One space dimension, *J. Comput. Phys.* 182 (2002) 516.
- [22] V.V. Rusanov, Calculation of interaction of non-steady shock waves with obstacles, *J. Comput. Math. Phys.* 1 (1961) 267.
- [23] A. Jameson, P.E. Vincent, P. Castonguay, On the non-linear stability of flux reconstruction schemes, *J. Sci. Comput.* doi:10.1007/s10915-011-9490-6.
- [24] P. Persson, J. Bonet, J. Peraire, Discontinuous Galerkin solution of the Navier–Stokes equations on deformable domains, *Comput. Method Appl. M* 198 (2009) 585.